INTERNATIONAL REVIEWS IN PHYSICAL CHEMISTRY, 1998, VOL. 17, NO. 2, 227–260

Photoelectron–photofragment coincidence studies of dissociation dynamics

by R. E. CONTINETTI

Department of Chemistry and Biochemistry, University of California, San Diego, 9500 Gilman Drive, La Jolla, CA 92093-0314, USA

Important insights into the energetics and dynamics of transient molecules and clusters have been obtained from studies of the photodetachment of negative ions. When photodetachment produces a neutral in a metastable or dissociative state, further information can be obtained by studying the subsequent dissociation dynamics of the molecule. This can be done by measuring the photoelectron kinetic energy and the photofragment translational energy release in coincidence. Energy- and angle-resolved measurements of this type are now possible in photoelectron–photofragment coincidence experiments. The photoelectron–photofragment coincidence technique is reviewed and the dissociative photodetachment (DPD) dynamics of O_4^-, O_3^-, $NO^-(N_2O)$ and $N_3O_2^-$ are discussed. These systems provide examples of direct and sequential DPD processes, along with applications to the study of isomeric forms of molecular and cluster anions.

1. Introduction

Photodetachment of negative ions has proven to be a valuable method for the study of the energetics and dynamics of transient neutral and ionic species. Laser photoelectron spectroscopy of negative ions has been used to measure electron affinities and to study the structure of molecules and clusters [1, 2]. In cases where photodetachment produces unstable neutrals, photoelectron spectroscopy has provided an approach to transition-state spectroscopy [3, 4] and insights into isomerization dynamics of polyatomic molecules [5]. When photodetachment produces a molecule in a dissociative excited state, or a weakly bound cluster far from the equilibrium geometry, rapid dissociation can occur. This is the process of dissociative photodetachment (DPD).

Characterization of the dynamics of DPD requires measurement of the kinetic energy and angular distributions, in coincidence, of the photoelectron and atomic or molecular fragments. The measured electron kinetic energy fixes the internal energy in the dissociative state. The subsequent dissociation dynamics of the energy-selected neutral can be analysed by photofragment translational spectroscopy. In this way, the dynamics of both photodetachment and the dissociation can be recorded and any correlation between the two processes can be determined directly. A new generation of lasers and particle detection techniques has now made experiments of this sort possible. This review will discuss some of the results obtained by this technique, photoelectron–photofragment coincidence spectroscopy, which combines the well established techniques of photoelectron spectroscopy [1] and photofragment translational spectroscopy [6] to perform kinematically well defined measurements in which the energies and recoil angles of a free electron and two photofragments are recorded in coincidence.

A topic closely related to DPD, but outside the scope of this review, is the dissociative photoionization of stable neutral molecules. Due to the need both to

0144–235X/98 $12.00

photoionize and dissociate the molecule, such studies typically require photon energies in excess of 10 eV. Particle detection is considerably simpler than in the case of DPD, since only charged products are detected. Thus, there have been many studies of dissociative photoionization, employing light sources ranging from discharge lamps to synchrotrons [7]. A number of coincidence techniques have been developed to carry out these studies [8]. For example, the angle-resolved photoelectron–photoion coincidence technique (AR-PEPICO) provides a similar level of information to that obtained in the photoelectron-photofragment coincidence experiments described here, since the energy and angular distributions of the photoelectron and the photoion are recorded in coincidence [9, 10]. There is much to be learned from studies of dissociative photoionization since the process is entirely analogous to DPD. The primary difference between the two processes is that the potential in the exit channel for photoionization is the long-range Coulombic interaction between the departing photoelectron and the positive ion core.

2. Photoelectron–photofragment coincidence spectroscopy

Photoelectron–photofragment coincidence spectroscopy can be understood by considering the schematic potential energy diagrams in figure 1. Figure 1(a) shows the potential energy of bound states of a diatomic anion and a ground state neutral as a function of internuclear distance. Assuming that one-electron photodetachment from the anion yields the electronic ground state of the neutral, photodetachment at low photon energies leads to a structured photoelectron kinetic energy (eKE) spectrum. The eKE spectrum shown in the figure assumes that the anion is in the vibrational ground state and the intensities of the peaks are determined by the Franck–Condon overlap of the vibrational wavefunctions in the two electronic states [1]. This is the type of experiment which has yielded so much information on the energetics and structure of transient neutral species by laser photoelectron spectroscopy of negative ions. Photodetachment to a metastable excited state of the neutral, shown in figure 1(b), can also produce a structured photoelectron spectrum which may yield considerable insight into the dynamics of the neutral excited state, including dissociation [4] and isomerization processes [5]. In this case photodetachment produces a bound excited state which subsequently predissociates, and this is referred to as sequential DPD. The photoelectron–photofragment coincidence spectrum can reveal the dissociation pathway and dynamics for the energy-selected neutral identified by detection of the photoelectron. Figure 1(c) shows a third limiting case: photodetachment to a repulsive state of the neutral. Here, measurement of the photoelectron spectrum still provides a measure of the vertical electron affinity of the neutral excited state, i.e. the energy by which the anion is stabilized relative to that state. The distribution of photoelectron kinetic energies should similarly be dictated by the Franck–Condon principal, although in that case one must consider bound–free Franck–Condon factors [11]. The photofragment translational energy release, E_T, provides additional information concerning the identity of the dissociation products and the repulsion between them. Thus, the coincidence experiment yields directly the energy required to produce a free electron and two photofragments from the stable anion. This process is referred to as direct DPD.

Sequential and direct DPD processes have distinctive spectroscopic signatures for a diatomic molecule. Figure 2 shows schematic photoelectron–photofragment correlation spectra. These are two-dimensional histograms showing the number of events with a given translational energy and photoelectron kinetic energy, $N(E_T, eKE)$.

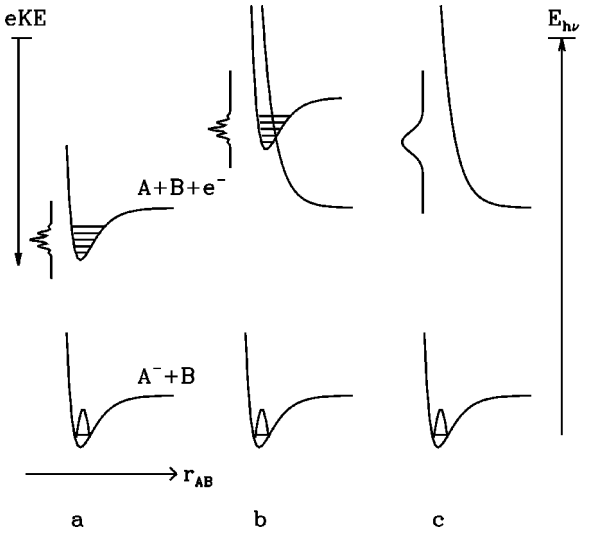

Figure 1. Schematic diagram of potential energy surfaces and photoelectron spectra for photodetachment and DPD processes of a hypothetical diatomic molecule as discussed in the text.

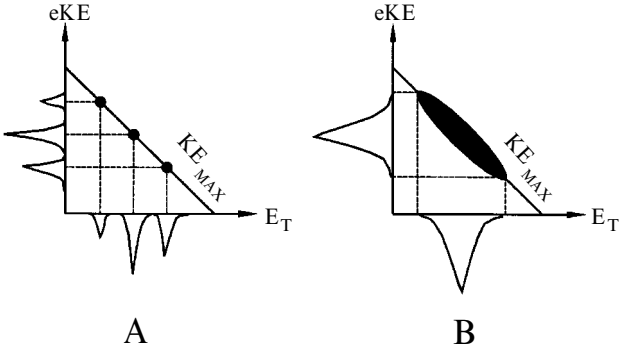

Figure 2. Schematic diagram of spectral signatures expected in a photoelectron–photofragment coincidence experiment for a diatomic molecule, showing the correlation expected between the photoelectron kinetic energy and the photofragment translational energy release. (A) Sequential DPD—photodetachment followed by predissociation. (B) Direct DPD.

Figure 2(A) shows the case of sequential DPD. The structured photoelectron spectrum is shown along the y axis. In this case, given the photon energy and the energy required to produce $A + B + e^-$, the maximum kinetic energy is fixed, and is shown as the diagonal line marked KE_{MAX}. Thus, in the absence of internal structure in A or B, each peak in the photoelectron spectrum will correspond to a peak along KE_{MAX}, and will inversely correspond to a peak in the E_T spectrum, i.e. a large eKE will correspond to a low E_T.

Figure 2(B) shows the case of direct DPD. Here the bound anion wavefunction is projected onto a repulsive excited state. The shape of the photoelectron spectrum is now determined by bound–free Franck–Condon factors. The breadth of the spectrum provides a direct measure of the slope of the repulsive surface given the bound-state wavefunction. A steeply sloped repulsive state will yield a broader photoelectron spectrum than a moderately sloped one. Since we are considering the dissociation of

a diatomic molecule, with no internal structure in the products, the $N(E_T, eKE)$ spectrum takes the form of a distribution along KE_{MAX}, with the inverse of the photoelectron spectrum appearing as the E_T spectrum.

Studies of DPD can be complicated by the diverse photochemistry exhibited by molecular anions. At low photon energies, molecular anions are subject to photodestruction by the competing processes of photodissociation and photodetachment. Photodissociation can occur by direct dissociation on a repulsive excited state, predissociation of an intermediate excited state, or dissociation on the ground state following internal conversion. Photodetachment can similarly proceed by several pathways [12]. A free electron and a stable neutral may be produced by either direct photodetachment or autodetachment of a metastable excited state. A DPD event will lead to the production of a free electron and two (or more) neutral photofragments. In this review, examples of DPD processes ranging from direct photodetachment with prompt dissociation on the timescale of molecular vibration to processes in which photodetachment is followed by a distinct dissociation step will be given. These DPD mechanisms are in contrast to the alternative route to neutral fragments and a free electron through photodissociation followed by autodetachment. In this process, electron departure occurs after the dissociation pathway has become well defined, and the electron kinetic energy spectrum can be expected to have a structure characteristic of the autodetachment process. In nature there is likely to be a continuum of timescales for these processes, leading to some situations in which a firm assignment to these limiting cases is difficult.

The initial studies of the DPD dynamics of small molecular and cluster anions carried out in our laboratory are reviewed here. The results obtained show how the dynamics of DPD can provide insights into the structure of molecular anions and the dissociative states of the corresponding neutrals. Removal of an electron from an anion with a significantly different geometry from the corresponding neutral species leaves the neutral in a highly repulsive region of the potential energy surface, leading to 'direct' dissociation which is typically characterized by a large release of translational energy. This behaviour is observed in the case of the DPD of O_4^- [13–17] and $N_3O_2^-$ [18]. An example of photodetachment to a metastable excited state, resulting in a sequential process, is provided by the DPD of O_3^- [19]. A third example involves cluster ions bound predominantly by weak electrostatic interactions. In this case photodetachment will access a weakly repulsive region of the neutral potential energy surface with a correspondingly small translational energy release between the photofragments. Dynamics consistent with this process have been observed for the $O_2^-(H_2O)$ [17, 20] and $NO^-(N_2O)$ [18] cluster ions. The $NO^-(N_2O)$ and $N_3O_2^-$ system provides an example of the sensitivity of the photoelectron–photofragment coincidence technique to the existence of isomeric forms of polyatomic anions.

2.1. *Experimental techniques*

Kinematic characterization of a DPD event requires the measurement, in coincidence, of the recoil angles and kinetic energies of the photoelectron and the photofragments. The apparatus developed to carry out the photoelectron–photofragment coincidence experiment combines established techniques in fast-ion-beam photofragment translational spectroscopy with a unique large-solid-angle photoelectron time-of-flight (TOF) spectrometer. The experimental methods are reviewed here, followed by a brief discussion of signal-to-noise considerations and data analysis methods.

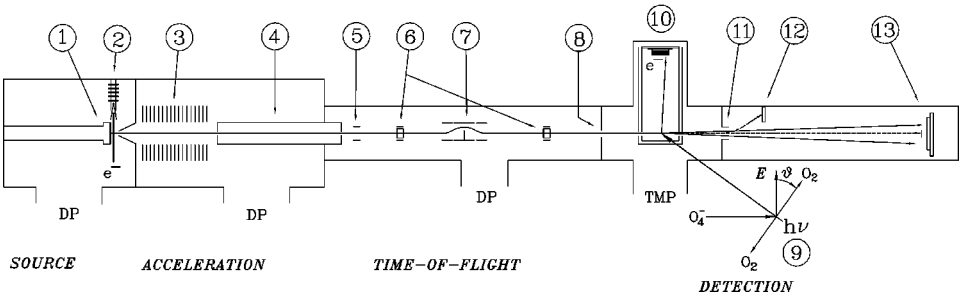

Figure 3. Schematic diagram of the apparatus, showing the primary regions and details of the ion source and TOF mass spectrometer. A vacuum is established by diffusion pumps (DPs) and a turbomolecular pump (TMP). See the discussion in the text for further details.

In addition to yielding novel insights into the dissociation dynamics of transient neutral species, studies of DPD entail significant experimental challenges. Detection of photoelectrons is relatively straightforward, however, detection of the neutral photofragments in coincidence poses a more difficult problem. Photoionization of the nascent neutrals is one possible approach, and has in fact been used in non-coincident measurements [21]. Coincidence measurements dictate that a technique with high detection efficiency be used. Detection of fast (laboratory kinetic energies > 1 keV) small neutral molecules such as those discussed in this review can be carried out with efficiencies of $\approx 50\%$ with microchannel-plate-based detectors [22]. The use of a fast negative ion beam has an additional advantage due to the fact that the photofragments are constrained to lie in a small cone in the forward direction along the ion beam for typical 'chemical' dissociation kinetic energies (< 4 eV). Thus, a relatively small-area detector can be used to detect nearly all of the neutral photofragments. For these reasons, a high energy ion beam (2–8 keV) apparatus was used to carry out measurements of the photofragments.

The choice of a fast ion beam poses specific challenges to performing high-resolution photoelectron spectroscopy. Detection of a large fraction of photoelectrons is necessary to make the coincidence measurement tractable. Use of a conventional large-solid-angle photoelectron detector such as a magnetic bottle [23] or a two-dimensional imaging technique [24, 25] is difficult, however, since such detectors do not permit straightforward measurement of the recoil angle of individual photoelectrons. When electrons are detected over a wide range of recoil angles from a fast ion beam, measurement of the recoil angle is essential to permit correction of the large Doppler shift produced by the velocity of the incident ion [26]. To carry out the measurement, a device which preserves the recoil angle of the photoelectron in addition to permitting measurement of the laboratory energy by TOF methods is required. Two approaches for collecting the photoelectrons, either a paraboloidal electrostatic mirror [27], or large-solid-angle TOF, coupled with a time- and position-sensitive photoelectron detector have been pursued in this laboratory.

As shown in figure 3, the apparatus is composed of an ion source, an acceleration region, a TOF region, and a detector region which contains the laser–ion-beam interaction volume and the particle detectors. The photoelectron [28] and photofragment translational [15] spectrometers have been independently described previously and will be reviewed in some detail here as applied to the photoelectron–photofragment coincidence experiment. The apparatus is differentially pumped, with

operating pressures of $1–5\times10^{-4}$ Torr in the source region, $2–8\times10^{-5}$ Torr in the acceleration region, 3×10^{-6} Torr in the TOF region and $\approx 1\times10^{-8}$ Torr in the detection region. The ion source and TOF mass spectrometer are discussed in more detail in the next section, followed by a description of the detector region.

2.1.1. *Ion sources and time-of-flight mass spectrometry*

A variety of pulsed ion sources could be applied in these experiments, however, all of the anions discussed in this review were produced by electron beam irradiation ((2) in figure 3) of a pulsed free-jet expansion (1). This has proven to be a versatile method of creating both positive and negative molecular and cluster ions [29]. An incident 1 keV electron beam is focused on the expansion, producing low-energy secondary electrons which attach to molecules via three-body collisional processes and by cluster evaporation [30]. The nascent anions, produced in the continuum flow region of the pulsed molecular beam, are subsequently cooled in the supersonic expansion. Vibrational temperatures in the 200–500 K region are typical for small molecular anions (O_3^-, CCO^-, N_3^-), while rotational temperatures < 50 K are expected for such systems [31]. O_4^- was produced by expansion of pure O_2 at a backing pressure of 1.5 atm. through a 0.25 mm piezoelectric pulsed nozzle operating at 600 Hz–1 kHz [32]. O_3^- was generated from a mixture of O_3 and O_2, while $NO^-(N_2O)$ and $N_3O_2^-$ were simultaneously generated by electron impact on pure N_2O.

The anions pass through a skimmer, enter a differentially pumped chamber, and are accelerated to an energy of 2.5–8 keV (3). A long-focal-length einzel lens embedded in the acceleration stack is used to optimize ion transport into the dissociation region. Shorter focal length elements are not used since it is necessary to maintain an ion beam with minimal angular divergence. After acceleration, the ion beam is re-referenced to ground potential using a high-voltage switch (4) [33]. This device is a stainless steel tube with small apertures at each end. Ions enter the tube while it is at the full acceleration potential, and it is then switched to ground before the ions exit. This procedure overcomes the need to float either the source or detector regions at the acceleration potential.

Ions that pass through the switch are mass selected using a TOF method due to Bakker [34]. A rapidly switched potential perpendicular to the beam axis (5) is used to permit only a small packet of ions to pass undeflected through a 1 mm entrance aperture to the detector region (8). After chopping the ion beam in this way, the ions separate into mass-selected packets by TOF. This approach was chosen as it induces minimal axial energy spread in the ion beam. The beam energy spread is estimated to be $\leqslant 5$ V, giving $\Delta E_{\text{beam}}/E_{\text{beam}} \leqslant 0.2\%$ and allowing accurate determination of the photofragment recoil energy and angles. Electrostatic deflectors (6) are used to transport the ion beam into the detection region. The ions are also guided over a beam-block [14] situated on the beam axis (7) which removes any fast neutral particles produced by collision-induced dissociation or detachment during acceleration [35].

2.1.2. *Photodetachment and detection of photoelectrons and photofragments*

A schematic diagram of the detection region of the apparatus is shown in figure 4. The mass-selected ion packets first pass through two 1 mm diameter defining apertures (8), then enter the ion-beam–laser interaction region by passing through a double mu-metal magnetic shield. The $\approx$ 1 mm diameter ion beam then is crossed by a pulsed laser focused to a $\approx$ 0.25 mm diameter spot (9). Due to the short flight path for the

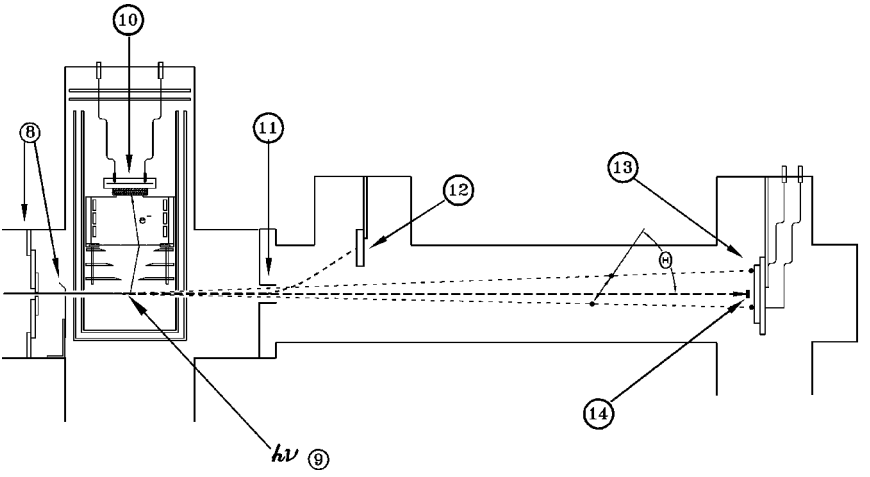

Figure 4. Schematic diagram of the detector region, showing the photoelectron and photofragment translational spectrometers as discussed in the text.

photoelectrons (7.5 cm), a short-pulse laser is required to permit accurate measurements of the photoelectron TOF. In the case of the experiments discussed here, a mode-locked, *Q*-switched, cavity-dumped Nd:YAG laser operating at a repetition rate of 1 kHz was used [36]. This laser produces $\approx$ 100 ps full-width-at-half-maximum (FWHM) pulses, with pulse energies of $\approx$ 150 μJ at 532 nm and $\approx$ 40 μJ at 355 and 266 nm. The laser is linearly polarized, and the polarization is rotated with the appropriate half-wave plates. The kinetic energy and recoil angle of a photoelectron which recoils into a cone centred above the crossing plane is measured (10). The nascent neutral and residual ions continue along the centreline of the apparatus. After exiting the magnetic shields, the residual ions are deflected out of the beam (11) into a simple microchannel-plate ion detector (12) used to monitor the ion beam intensity during the experiment. The two photofragments continue to recoil out of the beam path until they strike the two-particle photofragment detector (13).

2.1.3. *Photoelectron detection*

The photoelectron spectrometer employs a time- and position-sensitive electron detector to measure the laboratory kinetic energy by TOF and electron recoil angle by detected position. Measurement of the electron recoil angle is essential to allow correction for the Doppler broadening due to the fast ion beam [26]. With this correction, the electron kinetic energy in the centre-of-mass frame (*eKE*) is determined. Two techniques were used: a paraboloidal electrostatic mirror (PEM) [27] and a straight TOF method. The PEM, while collecting a large fraction of the photoelectrons, did not preserve the photoelectron recoil angle, thus limiting the resolution. Implementation of the PEM is described in detail in a previous publication [28], and was used to record the initial photoelectron-photofragment coincidence data on O_4^- [14]. The first version of the TOF photoelectron analyser [28] had a nominal field-free flight path of 150 mm and was used with a 6 ns pulse diode-pumped Nd:YLF photodetachment laser. Once the 100 ps photodetachment laser became available, this nominal flight path was reduced to the current value of 75 mm, increasing the collection efficiency by a factor of four.

The photoelectrons traverse a nominal field-free flight path of 75 mm and impinge on an 80 mm diameter detector entrance grid centred above the laser–ion-beam interaction region. The photoelectron is then accelerated to 300 V and focused onto the 40 mm diameter time- and position-sensitive detector (10). This microchannel-plate-based detector uses a wedge-and-strip anode [37] to record the time- and position-of-arrival of the photoelectron. Standard charge analysis and constant-fraction-discriminator timing techniques are used to achieve a detector spatial and temporal resolution of ≈ 100 μm and 0.5 ns, respectively. The data are transferred to a personal computer and stored as four 13-bit integers containing the charge and time-to-amplitude converter data required to determine the x,y and TOF of each photoelectron. These data are serially stored with the photofragment data described below. From this information, the flight path, laboratory energy and recoil angle are calculated for each photoelectron, yielding the centre-of-mass electron kinetic energy (eKE).

Aberrations in focusing the photoelectrons onto the detector limit the centre-of-mass eKE resolution to $\approx 4\%$ $\Delta E/E$, and an effective angular acceptance of $\approx 4\%$ of 4π sr. Calibration by the photodetachment of O_2^-, NO^-, O^- and I^- has shown that peaks in the photoelectron spectra can be measured with an accuracy of $\approx 1.5\%$.

2.1.4 *Photofragment detection*

If the neutral species dissociates, the photofragments recoil out of the beam and impinge on a two-particle time- and position-sensitive detector (13). The nominal flight path from the laser interaction region to the photofragment detector is 0.96 m. The photofragment detector is similar in design to the split wedge-and-strip anode developed by Continetti *et al.* [38], however, it is capable of measuring either neutral or ionic photofragments. The photofragments that clear a beam-block (14) 4.5 mm wide with a 7 mm diameter central spot impinge on the photofragment detector. The beam-block is required to prevent a single photofragment from exciting both halves of the detector, and results in an effective dead area. Measurement of the time- and position-of-arrival of the photofragments allows determination of the mass, centre-of-mass (CM) translational energy (E_T) and recoil angle of each fragment, as originally described by DeBruijn and Los [39] and also in reference [38]. Studies of the photodissociation of O_2^- have shown that the translational energy resolution is $\leqslant 10\%$ $\Delta E/E$ at $E_T = 0.55$ eV integrated over the entire detector active area, and the accuracy is $\approx 2\%$ [15]. Due to the required beam-block, the angular acceptance of the detector is a function of beam kinetic energy, product mass ratio and translational energy release. Depending on the translational energy release and the kinematics, the beam energy and/or the flight path can be adjusted to illuminate optimally the 40 mm diameter photofragment detector. In the case of O_4^- dissociation into $O_2 + O_2 + e^-$ at 532 nm, the detector accepts $\approx 80\%$ of the coincident photofragments. The efficiency drops to $\approx 50\%$ of 4 π sr given the kinematics of $O + O_2$ dissociation at 266 nm.

Photofragments are determined to originate from a single dissociation event by checking for conservation of linear momentum in the CM frame. Conservation of linear momentum also serves to determine the photofragment mass ratio. This must be done for all possible product channels. Events are rejected if the apparent CM of the two fragments at the detector is located outside an approximately 2 mm^3 volume defined by the projection of the laser–ion-beam interaction volume onto the detector. Correlation of the photoelectron and the neutral photofragments is determined by the spectrometer efficiency and the count rate as discussed below.

2.1.5. *Signal-to-noise ratio*

The calculation of the rate of detection of true coincidences was an important consideration in the design of this experiment. Using the Nd:YAG laser discussed above it is possible to obtain more than one detachment event per laser shot for systems with large photodetachment cross sections ($\sigma = 10^{-16}$ cm^2) given ion-beam number densities of the order of 10^6 cm^{-3}. In many cases, however, the photodetachment cross sections are smaller and the ion beam densities may be considerably lower. This is sometimes advantageous, however, as consideration of false three-particle coincidences dictates that lower event rates are required—no more than 0.1 detachment/dissociation events per laser shot on average. In this case, Poisson statistics indicate that the probability of a single event occurring is $P(1) \approx 0.09$ per laser shot. The detection efficiency for each of the neutral fragments (f_n) and the photoelectron (f_e) should be $\approx 50\%$ with the microchannel-plate detectors [22]. If we assume that the photofragment detector geometry allows 50% of the photodissociation events to be collected in coincidence, ($\Delta\Omega_n$), and 4.25% of the electron solid-angle ($\Delta\Omega_e$) is collected with a transmission efficiency (T_e) of 81%, the average number of successful triple-coincidences per laser shot will be

$$n_{tco} = P(1)\,(f_n^2\,\Delta\Omega_n)\,(f_e\,\Delta\Omega_e\,T_e) \approx 0.0002, \tag{1}$$

giving a signal count rate of 0.2 Hz when the experiment is run at 1 kHz.

Consideration of sources of background and false coincidences is also important in the design of this experiment. Multiple-event false coincidences can be eliminated by hardware and software charge-discrimination techniques. The most important source of random noise is correlated with the photoelectron signal in time, resulting from stray photoelectrons produced by laser light or the incident ion beam striking surfaces in the analyser. The ion background has been eliminated by better collimation of the incident ion beam with a second 1 mm aperture. The laser-correlated background has a common signature of being an increasing signal at low *eKE*, and only becomes a serious problem at 266 nm.

The most fundamental type of noise in a coincidence experiment of this type is false coincidences. Many of these will be eliminated due to the fact that the neutral particle detection scheme allows determination that the two photofragments are from the same dissociation event by the conservation of momentum. Thus, the important false coincidences to consider are those events in which only the detected photoelectron is not correlated with the coincident neutral fragments. The rate of these false coincidences is given by

$$n_{fco} = P(2)\,2\,(f_n^2\,\Delta\Omega_n)\,(1-f_n^2\,\Delta\Omega_n)\,(f_e\,\Delta\Omega_e\,T_e)\,(1-f_e\,\Delta\Omega_e\,T_e) = 1.7\times10^{-5} \tag{2}$$

where $P(2) = 0.016$ is the probability for two detachment events occurring per laser shot when the average number of events per shot is 0.1. The term proportional to f_n^2 accounts for the probability of detecting two correlated fragments out of the four fragments produced in two dissociative events, with multiplication by two accounting for the fact that there are two correlated ways of doing this. The term proportional to f_e accounts for the probability of detecting only one out of the two photoelectrons. The $(1-f)$ terms account for the fact that the remaining photofragments and photoelectron are not detected. This expression gives a false coincidence count rate of 0.017 Hz when the experiment is run at 1 kHz, approximately 8% of the true coincidence count rate.

The required data acquisition time for a photoelectron–photofragment coincidence experiment can now be estimated. If the interesting region of the photoelectron spectrum covers 1 eV, there will be 25 electron kinetic energy bins, each 40 meV wide. If only one dissociation channel is operative at a given electron kinetic energy and the fragment kinetic energy distribution is recorded over 2 eV in 50 meV wide bins, there will be 40 fragment translational energy release bins, giving a total of 1000 $N(E_T, eKE)$ bins to fill. Assuming the signal is evenly distributed, and 100 events per channel are desired for 10% counting statistics, 1.0×10^5 events (140 h of data acquisition) would be required. In the examples reviewed here, $2\times 10^4 - 4\times 10^4$ three-particle coincidences were obtained, with acquisition times ranging from 30–60 h. Improvements in photoelectron detection efficiency are required to reduce these counting times significantly.

2.1.6. *Data analysis*

The raw data obtained in these experiments are converted to time- and position-of-arrival (x, y, t) information for each detected particle off-line, yielding directly the raw CM photoelectron and photofragment translational energy and angular distributions recorded in the experiment. The energy and angular distributions can be corrected for the finite angular acceptance of the detectors using a straightforward numerical procedure [15, 17, 20, 38]. This involves calculating the fraction of events which can be detected in coincidence as a function of CM translational energy, E_T and polar CM scattering angle, θ, given the finite laboratory angular acceptance of the detector. The raw data are then divided by this detector acceptance function, to yield the acceptance-corrected CM translational energy and angular distribution $P(E_T, \theta)$. The $P(E_T, \theta)$ is interpreted using a least-squares fit to the standard electric dipole model [40, 41]. The model describes the CM translational energy and angular distributions in a separable approximation as

$$P(E_T, \theta) = P(E_T)[1 + \beta(E_T) P_2(\cos\theta)]. \quad (3)$$

Here, $P_2(\cos\theta)$ is the second Legendre polynomial in $\cos\theta$, and θ is the angle between the fragment recoil direction and the electric vector of the laser. $\beta(E_T)$ is the energy-dependent anisotropy parameter describing the angular distribution and $P(E_T)$ is the CM translational energy distribution. $\beta(E_T)$ in this formula can range between the 'parallel' ($\beta = 2$, or $\cos^2\theta$) and 'perpendicular' ($\beta = -1$, or $\sin^2\theta$) limits [40]. In the case of photoelectron–photofragment coincidence data, the raw energy correlation spectra between the photoelectron and photofragments are typically reported. Extraction of photoelectron–photofragment angular correlations requires correction for the detection efficiency as discussed below in the case of O_4^-.

3. Direct dissociative photodetachment: O_4^-

The dimer anion of oxygen, O_4^-, provides the most striking known example of a direct DPD process. As will be illustrated below, the dynamics exhibited by this system approximate those of a diatomic molecule. This is a result of two important factors. First, O_4^- is bound by 0.46 eV relative to $O_2 + O_2^-$, while the low-lying states of O_4 are strongly repulsive at the geometry of O_4^-. Second, the structure is characterized by a high degree of symmetry due to delocalization of the excess electron. This results in a case where only a very narrow range of product O_2 rotational states are populated in DPD. An additional point of interest arises due to the rapid dissociation and the

symmetry of the system—a strong molecular frame anisotropy is observed in the photoelectron angular distribution. These features of O_4^- taken together yield a system which provides a beautiful proof-of-principle experiment for the technique of photoelectron–photofragment coincidence spectroscopy.

Several studies of the photodestruction dynamics of O_4^- were carried out in the 1970's, due to interest in the role this ion plays in mediating the electron density in the ionosphere [42]. This work showed that the photodestruction cross section exhibited no fine structure, and Lee and Smith [43] proposed that this might be a consequence of DPD. More recently, O_4^- has been studied using photoelectron spectroscopy [44] and translational energy spectroscopy [13, 15].

The primary concern in this review is the photodestruction processes of O_4^- at 532 nm. At this wavelength, it has been shown that both photodissociation ($O_4^- + h\nu \rightarrow O_2^- + O_2$) and DPD ($O_4^- + h\nu \rightarrow O_2 + O_2 + e^-$) processes occur [15, 44]. Photodissociation at 532 nm has been observed to predominantly yield (90%) $O_2(a^1\Delta_g) + O_2^-(X^2\Pi_g)$, resulting in a sharp peak in the E_T spectrum at 0.8 eV. The angular distribution of the photodissociation products is strongly peaked along the electric vector of the laser, showing that photodissociation occurs via a prompt parallel transition [15]. The dominant feature in the E_T spectrum, however, is a broader peak centred at 0.4 eV, which has been shown to arise from DPD. The angular distribution of the O_2 products of DPD is strongly peaked perpendicular to the electric vector of the laser [13].

The photoelectron kinetic energy spectrum at 532 nm shows a broad, structureless peak centred at 0.7 eV with a FWHM of 0.3 eV. This structureless spectrum is in marked contrast to the vibrationally resolved photoelectron spectrum of O_2^- at this wavelength, showing that the structure of O_4^- cannot be described as a weakly interacting O_2–O_2^- complex. Similar to the molecular products of DPD, the photoelectron angular distribution is also peaked perpendicular to the electric vector of the laser beam [44]. In the next section we consider the additional insights to be gained from photoelectron–photofragment coincidence experiments.

3.1. *Photoelectron–photofragment energy correlations*

The (E_T, eKE) correlation spectrum is shown in figure 5. In addition to the two-dimensional correlation the photoelectron and photofragment translational energy release spectra are shown along the y and x axes respectively. These one-dimensional spectra are obtained by integrating the correlation spectrum over the complementary variable. The correlation spectrum itself is represented as a contour map of the number of events $N(E_T, eKE)$, and reveals a series of five diagonal ridges, centred at E_T = 0.4 eV and a vertical row of spots at E_T = 0.8 eV. The eKE values of the spots in the vertical row at E_T = 0.8 eV are consistent with the known eKE peaks in the O_2^- photoelectron spectrum [45]. These features arise from a second photon detaching the electron from an $O_2^-(X^2\Pi_g)$ photofragment produced in the photodissociation of O_4^-.

The diagonal ridges are the most interesting features in this correlation spectrum. Energy conservation dictates that all events that lie within a single diagonal ridge have a well defined total kinetic energy, ($E_{TOT} = E_T + eKE$). Within a given ridge, however, there is a range of kinetic energy partitioning between the three products ($2O_2 + e^-$). Given the dissociation energy of O_4^- into $O_2(X^3\Sigma_g^-) + O_2^-(X^2\Pi_g)$ (0.46 eV, [46]) and the electron affinity of O_2 (0.45 eV, [45]), the maximum translational energy for the DPD $O_4^- + h\nu \rightarrow O_2(X^3\Sigma_g^-) + O_2(X^3\Sigma_g^-) + e^-$ at 532 nm is 1.42 eV. This is marked as limit A on figure 5.

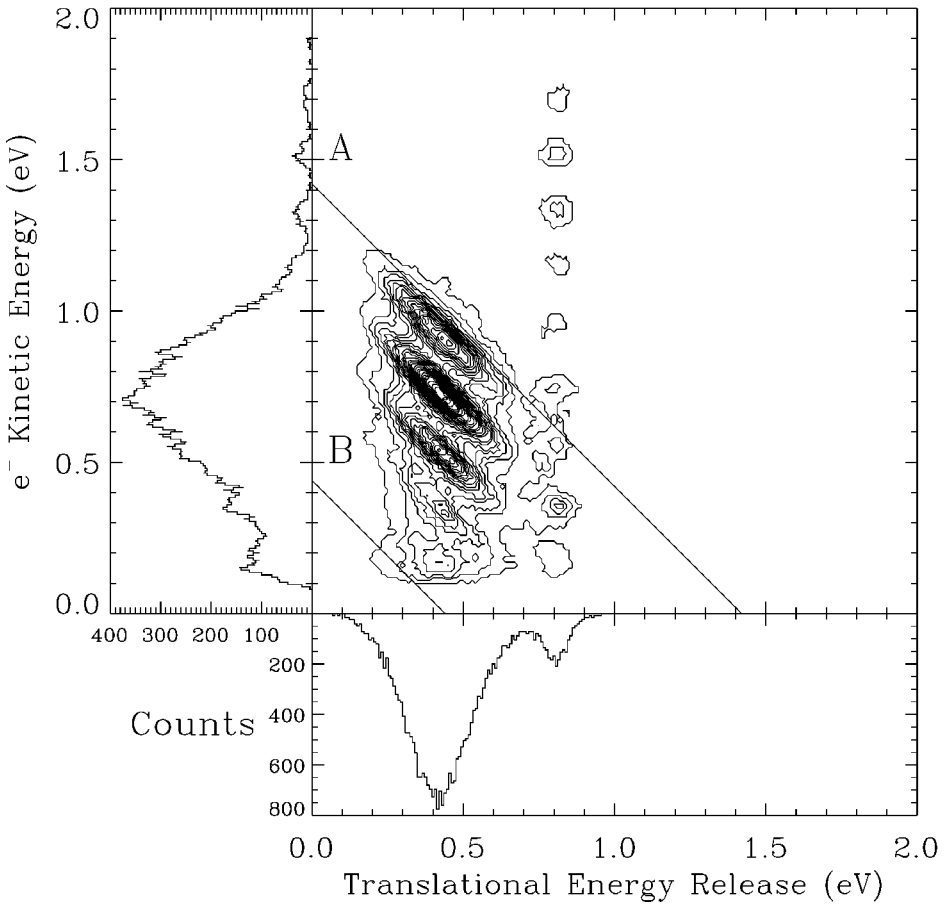

Figure 5. $N(E_T, eKE)$ correlation spectrum of the photoelectron electron kinetic energy and the translational energy release for O_4^- at 532 nm (2.33 eV). Contours are linearly spaced, with intensity representing the number of coincident events. Energetic limits are shown for A, $O_2(X^3\Sigma_g^-) + O_2(X^3\Sigma_g^-) + e^-$; and B, $O_2(X^3\Sigma_g^-) + O_2(a^1\Delta_g) + e^-$. The photoelectron and photofragment translational energy spectra are shown along each axis.

The diagonal ridges are spaced by product O_2 vibrational quanta. The product O_2 vibrational distribution can be examined quantitatively by considering the one-dimensional spectrum of the total kinetic energy release, E_{TOT}. As the E_{TOT} spectrum in figure 6 shows, the diagonal ridges in the correlation spectrum of figure 5 appear as well resolved peaks. The limit A is shown as a vertical line in figure 6 and corresponds to the origin of the internal energy axis shown at the top of the figure. The spacing of the first five vibrational levels of O_2 are shown as combs on the spectrum for reference. The offset of the vibrational peaks from the internal energy origin gives an average rotational energy of the photofragments of 80 ± 30 meV. The width of these peaks indicates a narrow range of rotational excitation for the two O_2 products, implying that O_4^- dissociates from a well defined structure.

The observation of vibrational structure in the E_{TOT} spectrum allows structural inferences on gas-phase O_4^- to be made. If we assume that O_4^- is composed of two distinct O_2 moieties, a simple simulation can be done by calculating the Franck–Condon overlap of the vibrational wavefunctions of two perturbed O_2 molecules with

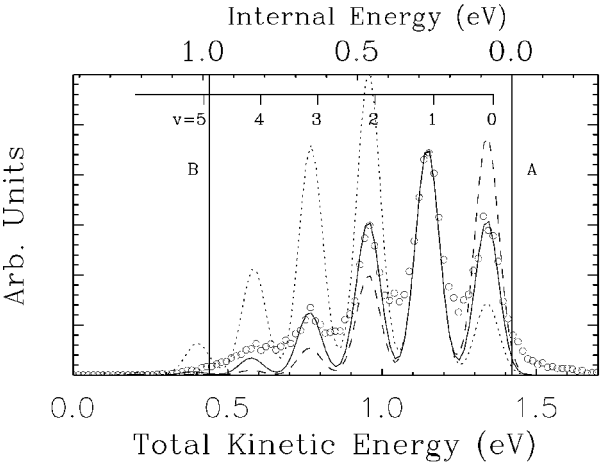

Figure 6. Total kinetic energy spectrum for DPD events. Energetic limits are the same as those shown in figure 1. The top axis indicates the internal energy. The data are represented by open circles; the full curve fit to the data assumes two equal bond length O_2 moieties of 1.272 Å; the dotted curve fit assumes unequal O_2 moiety bond lengths of 1.23 Å and 1.33 Å; the dashed curve fit assumes equal bond lengths of 1.26 Å. The fits are normalized to the $v = 1$ peak.

two free $O_2(X^3\Sigma_g^-)$ (r_e = 1.207 Å [47]). This separable approximation assumes that the nascent O_2 photofragments formed upon photon absorption are non-interacting diatomic molecules. Franck–Condon factors for each energetically allowed combination of vibrational states can then be calculated as products of the individual diatomic Franck–Condon factors. The results of this calculation are plotted as the solid curve in figure 6. The agreement between the simulation assuming equal bond lengths of 1.272 Å and the data is excellent. The sensitivity of the simulation to changes in the bond lengths of the perturbed O_2 is shown by the textured curves in figure 6. The 1.272 Å O–O bond length is midway between O_2^- and O_2, indicating that the excess electron is delocalized. In addition, the observation of a narrow rotational distribution among the O_2 products implies that O_4^- has a well defined symmetric structure. Recent matrix-isolation studies coupled with density functional calculations [48] and multiconfigurational *ab initio* calculations [49] have converged on a D_{2h} minimum energy structure for O_4^- which is consistent with our observations.

Extending the separable model of the previous paragraph, let us now model O_4^- as a pseudo-diatomic molecule. If we consider the O_2–O_2 distance in O_4^- as a bound coordinate, the slope of the repulsive O_2–O_2 potential energy surface can be inferred from the (E_T, eKE) correlation spectrum. In the absence of energy transfer in the exit channel, the diagonal lines observed in the (E_T, eKE) correlation spectrum result from projection of the wavefunction describing bound O_4^- onto the repulsive potential describing $O_2 + O_2 + e^-$ in a bound-to-free Franck–Condon transition [11]. Since the lines are diagonal, the widths of the projections onto either the eKE or E_T axes are identical. The length of the projection is a function of the slope of the repulsive potential which governs the dissociation of neutral O_4. The steeper the slope of the repulsive potential, the longer the ridge in the (E_T, eKE) correlation spectrum. The data shown here are consistent with projection of the bound O_2–O_2 wavefunction onto a ladder of vibrationally adiabatic repulsive curves leading to the O_2 product vibrational states. Implicit in this model is that there is no energy transfer between the

dissociating O_2 molecules. The simple separable model described here provides a reasonable interpretation of the observed dissociation dynamics and insights into the gas-phase structure of O_4^-.

3.2. *Photoelectron–photofragment angular correlations*

Photoelectron angular distributions provide detailed information on photodetachment dynamics due to the fact that they are a function of both the magnitude and relative phases of the degenerate angular momentum states of the electron continuum accessible in photodetachment processes [50, 51]. Studying the photoelectron angular distribution in the molecular frame can provide greater insights into the photodetachment dynamics, due to the removal of averaging over molecular orientations inherent in a laboratory angular distribution. Theoretical studies of such molecule-fixed photoelectron angular distributions (MF-PADs) have been pursued for an improved understanding of the dynamics of photoionization [50, 52, 53, 54, 55] and electron interactions with molecules oriented on surfaces [56]. Manifestations of the MF-PAD have been observed in experiments on the dissociative photoionization of H_2 [57], O_2 [58], N_2 [10], several halomethanes [9, 59] and dissociative electron-impact phenomena [60]. Detailed measurements of the MF-PAD in the photoionization of NO have recently been reported [54].

Measurements of the MF-PAD for the photodetachment of negative ions are of interest as they provide insight into the nature of both the bound electron in the anion and the anisotropy of electron–molecule interaction potentials. Due to the rapid dissociation of O_4 and the highly anisotropic O_2 product angular distributions, angle-resolved photoelectron–photofragment coincidence experiments provide an ideal method to search for manifestations of the MF-PAD. The angular distributions of the $O_2 + O_2 + e^-$ photoproducts are observed to be highly anisotropic. Both photoelectrons and O_2 photofragments produced in the DPD of O_4^- are preferentially scattered in the plane perpendicular to the **E** vector ($\beta \approx -0.8$ and -0.5 for photofragments and photoelectrons respectively) [15, 17].

In these experiments, the recoil angles for the photoelectron and photofragments are measured in coincidence, yielding the angular correlation between these three particles and the **E** vector. A pronounced angular correlation is observed which may be understood by considering figure 7, which shows surface density plots of the O_2 photofragment angular distribution both with and without coincident detection of the photoelectron. In reference [16], results obtained with only one orientation of the photofragment beam-block were reported. The results shown here represent experiments done with two orientations of the detector beam-block, leaving only a central core undetectable. The effect of the detector acceptance on an isotropic distribution is shown in figure 7(D), which also shows the geometry of detection, with the **E** vector parallel to the ion beam. The E_T-integrated DPD photofragment angular distribution, $N_n(\theta, \phi)$, is extracted by integrating the data over $0 < E_T < 0.6$ eV to give the number of events as a function of θ and ϕ. In this notation, n denotes the number of particles detected in coincidence ($n = 2$ for $O_2 + O_2$ and $n = 3$ for $O_2 + O_2 + e^-$) and θ, ϕ are the polar and azimuthal angles around the **E** vector respectively. Figure 7(A) shows a surface density plot of $N_2(\theta, \phi)$. Since the O_2 photofragment angular distribution is nearly $\sin^2\theta$, with $\beta = -0.8$, this resembles a torus. Detection of an electron in coincidence requires that the electron recoil into a cone above the plane of the laser and ion beam, breaking the cylindrical symmetry about the **E** vector and the ion beam. The effect of the angular correlation between the photofragments and photoelectrons

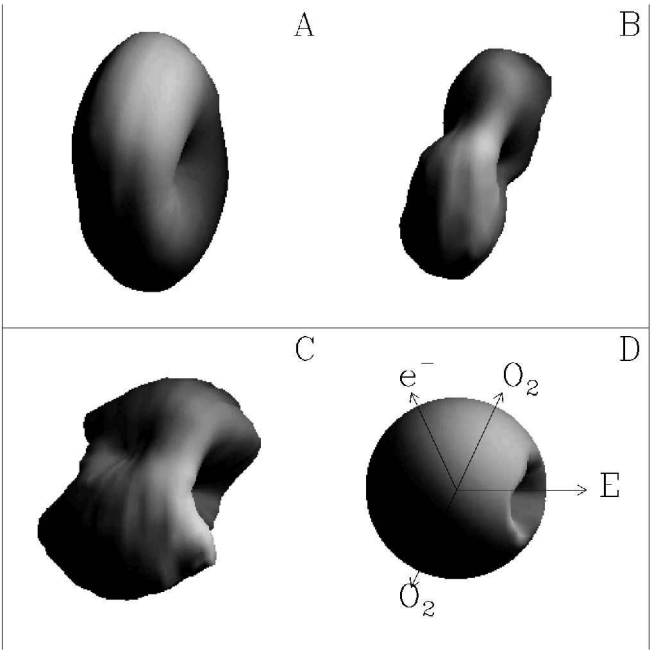

Figure 7. Surface density plots of the energy-integrated angular distributions of O_2 photofragments. The number of events is shown as the distance of the surface from the origin. Frame (A) shows the experimentally observed photofragment distribution $N_2(\theta, \phi)$ for detection of coincident O_2 photofragments. Frame (B) shows the experimentally observed photofragment distribution $N_3(\theta, \phi)$ for the coincident detection of two photofragments and an electron. Frame (C) shows the photofragment distribution relative to the electron ejection direction $N_3(\theta, \phi)/N_2(\theta, \phi)$. Frame (D) shows the nominal direction of the **E** vector, the photoelectron and photofragment recoil directions and the effect of the detector acceptance on an isotropic product angular distribution.

is shown in figure 7(B). This figure shows $N_3(\theta, \phi)$, the angular distribution for the O_2 photofragment pairs in the $O_2 + O_2 + e^-$ coincidence data. A pronounced reduction of $O_2 + O_2$ photofragment recoils detected parallel to the direction of electron detection ($\theta \approx 105^\circ$ in the CM frame) is observed. The existence of this angular correlation shows that photodetachment and dissociation of the nuclear framework of O_4 both occur on timescales fast relative to molecular rotation ($\approx$ 1–10 ps). Thus, by measuring the asymptotic recoil direction of the O_2 photofragments, the spatial direction of the dissociating bond at the time of photon absorption is determined. These results show that the photoelectron preferentially recoils *perpendicular* to the breaking bond in O_4.

This angular correlation is an obvious manifestation of an anisotropic MF-PAD. As first discussed by Dill [52] in reference to the photoionization of diatomic molecules, the MF-PAD contains considerably more information than the laboratory angular distributions. In contrast to equation (3), which describes electric dipole laboratory angular distributions, Dill showed that the MF-PAD will in general be described by

$$\frac{d\sigma}{d\Omega} = \sum_{l=0}^{2l^*} \sum_{m} A_{lm} \, Y_{lm}(\vartheta, \varphi) \tag{4}$$

In this equation, l^* is the maximum value for the photodetached electron orbital angular momentum and m corresponds to the azimuthal quantum number for the

photodetached electron. The magnitudes of the coefficients A_{lm} are determined by electric dipole selection rules and interference between the degenerate photoelectron continuum channels. These coefficients thus contain detailed information on both the photodetachment dynamics and the orbital from which the electron is ejected, determining the relative contributions of the spherical harmonics Y_{lm}, which are referenced to the molecular frame by the polar and azimuthal angles ϑ and φ. The strong angular correlation observed between photoelectron and photofragments indicates that the photoelectron continuum (and the expansion in equation (4)) is dominated by a restricted set of partial waves. Direct extraction of the MF-PAD requires further modelling of the photoelectron detector angular acceptance. A detailed theoretical treatment of the MF-PAD in the photodetachment of O_4^- requires a much more thorough understanding of the electronic structure of this radical anion than is now available.

The nature of the photoelectron–photofragment angular correlation can be further visualized by considering the photofragment angular distribution in the electron recoil frame, as opposed to the **E** vector frame. This distribution can be easily generated by dividing $N_3(\theta, \phi)$ by $N_2(\theta, \phi)$. This has the effect of removing from $N_3(\theta, \phi)$ weighting due to both the photofragment angular distribution in $N_2(\theta, \phi)$ and the finite angular acceptance of the photofragment detector. This treatment presumes that the photoelectron recoils at a single nominal angle in the laboratory frame. As the distribution in figure 7(C) shows, the electron recoil frame photofragment angular distribution also resembles $\sin^2\theta$, however it is now referenced to the electron-recoil direction. A fit to equation (1) shows that this distribution is characterized by $\beta \approx -0.5$. Due to the assumption of a nominal electron recoil laboratory angle, this is an upper bound on this anisotropy parameter.

In summary, due to the rapid dissociation of O_4^- after photon absorption, measurement of the photoelectron and photofragment translational energies in coincidence is required to reveal the energy partitioning to vibrational degrees of freedom of the O_2 products. A simple Franck–Condon model shows that the product vibrational distribution is sensitive to the structure of O_4^-. A striking angular correlation is observed between the photoelectron and the photofragments. Detailed information on the electronic structure of this open-shell negative ion is required to apply the existing formalisms for the MF-PAD to the DPD of O_4^-.

3.3. *Wavelength dependence of dissociative photodetachment of O_4^-*

Recent studies of the wavelength dependence of the DPD of O_4^- have confirmed that the dominant behaviour is well-described by a Franck–Condon-like process at 523, 355, 349, 266 and 262 nm [14, 17]. However, there is one exception to this simple picture—a significant non-Franck–Condon process observed at 349 nm [14] and also weakly at 355 nm. This is shown clearly in the photoelectron–photofragment correlation spectrum in figure 8, recorded at lower resolution using the PEM photoelectron spectrometer. At 349 nm, there are two peaks in both the photoelectron spectrum and the translational energy release spectrum. These pairs of peaks become three distinct features in the correlation spectrum. One of the features appears just below the energetic limit (B) for the production of $O_2(^3\Sigma_g^-) + O_2(^1\Delta_g) + e^-$. The most surprising result, however, is that two features appear in the region where only $O_2(^3\Sigma_g^-) + O_2(^3\Sigma_g^-) + e^-$ products are allowed. Feature 1 is related to the Franck–Condon feature observed at 523 nm [14] and, with higher resolution at 532 nm in

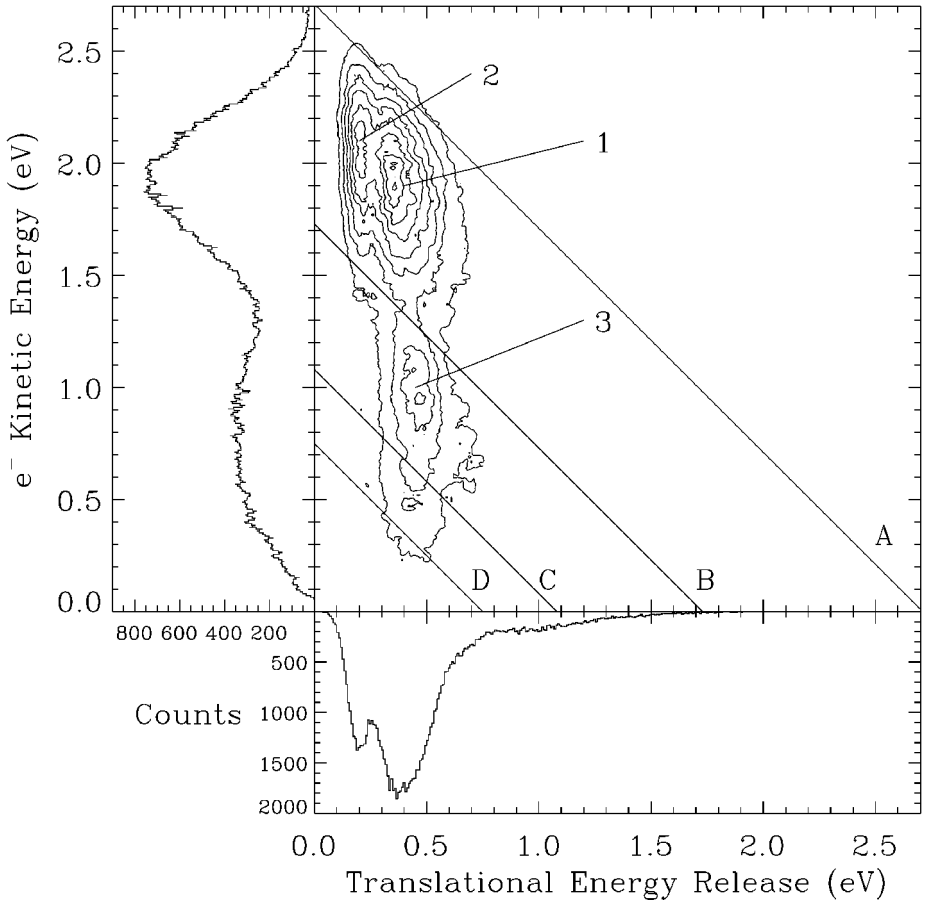

Figure 8. $N(E_T, eKE)$ correlation spectrum of the photoelectron electron kinetic energy and the translational energy release for O_4^- at 349 nm. Contours are linearly scaled, with the intensity representing the number of coincident events. Energetic thresholds are shown for: A, $O_2(^3\Sigma_g^-)+O_2(^3\Sigma_g^-)+e^-$; B, $O_2(^3\Sigma_g^-)+O_2(^1\Delta_g)+e^-$; C, $O_2(^3\Sigma_g^-)+O_2(^1\Sigma_g^+)+e^-$; D, $O_2(^1\Delta_g)+O_2(^1\Delta_g)+e^-$. The features labelled 1, 2 and 3 are discussed in the text.

figure 5. The centroid of the translational energy for this feature in unchanged and the peak photoelectron energy is increased by the difference between the photon energies. Feature 2, however, is characterized by a lower translational energy and a slightly higher photoelectron energy. Since no low translational energy peak was observed at 532 or 523 nm, it is impossible to account for this peak within the Franck–Condon approximation. It is likely that this feature arises from an electron–molecule scattering resonance embedded in the continuum. Numerous resonances have been found in low-energy $e^- - O_2$ scattering experiments by Spence and Schulz [61]. The $(A^2\Pi_u)$ state of O_2^- is expected to lie ≈ 3.1 eV above $O_2^-(X^2\Pi_g)$ [47]. A perturbed analogue of this state may be imbedded in the $O_2+O_2+e^-$ continuum at the energy reached by photodetachment at 349 nm. Thus, this non-Franck–Condon feature may result from the decay of a short-lived electron–molecule scattering resonance or autodetaching state. The possibility of structure in the continuum is one that always must be considered in cases of direct DPD.

4. Sequential dissociative photodetachment: the low-lying excited states of O_3

The DPD of the low-lying excited states of O_3 provides the best example of a sequential process in which electron departure and dissociation of the molecular frame are distinct, uncoupled events. O_3 provides a particularly inviting target for study by photoelectron–photofragment coincidence spectroscopy due to the existence of several low-lying excited states. Figure 9 shows an energy level diagram for O_3^- and O_3, and provides an illustration of the advantage that negative-ion photodetachment provides for the study of optically forbidden excited states. Optical excitation of the $^1A_2$ state is dipole forbidden from the $^1A_1$ ground state, and the three low-lying triplet states are also optically forbidden. While these states have been studied by absorption techniques [62, 63], their small optical cross sections have prevented any measurements of the dissociation dynamics. This is in stark contrast to the numerous studies of the singlet states of O_3 [64]. Photodetachment of the $^2B_1$ ground state of O_3^-, on the other hand, can produce all of these states by fully allowed one-electron transitions. This has led to several studies of the energetics and structure of the excited states of O_3 by electron scattering [65, 66, 67, 68] and photodetachment [69, 70] experiments. Recently, Arnold *et al.* [71] reported high-resolution photoelectron spectra that reveal features assigned to the five lowest excited states of O_3. Thus, it was clear that O_3^-/O_3 would make a good system for study by the photoelectron–photofragment coincidence technique.

The energetics and dynamics of the low-lying excited states of O_3 are also of considerable interest due to the important role played by O_3 in atmospheric chemistry. In particular, there has been interest in the possible existence of bound excited states of O_3. Kinetic studies have suggested that a bound low-lying excited state may explain discrepancies observed in measured rates of ozone production through the important three-body recombination reaction $O + O_2 + M \rightarrow O_3 + M$ [72]. A metastable singlet state of D_{3h} symmetry has been predicted to exist [73–76] and may play a role in this reaction. This species has yet to be observed. There are, however, the three known low-lying triplet states ($^3A_2$, $^3B_2$, and $^3B_1$) which are poorly characterized. Recent experimental studies have indicated that these states lie above the energy required for dissociation of O_3 into ground state $O + O_2$ products [63, 77, 71] as shown in figure 9. These states have recently been studied by multiconfigurational perturbation theory calculations by Tsuneda *et al.* [78] and Borowski *et al.* [79]. Their results support the assignments of Arnold *et al.* [71] except for the $^3B_1$ and $^3B_2$ states which the calculations show to be nearly degenerate.

Recent theoretical and experimental studies have suggested that the low-lying triplet states may explain vibronic structure in the Wulf band [80–84]. High-sensitivity absorption spectroscopy [63, 77, 82] has been used to study these very weak transitions. Recent work by Bouvier *et al.* [77] has provided high-resolution absorption spectra from 8600–10 500 cm^{-1}. These spectra reveal rotational structure superimposed on the origin and first bending vibration transitions, assigned to the $^3A_2$ electronic state [77]. An estimated radiative lifetime of 0.01–0.1 s for this state was obtained from the Einstein coefficients and Franck–Condon factors with the ground state of O_3 [77]. This is an upper limit to the actual lifetime. Pressure and Doppler broadening in these experiments prevented measurement of reliable homogeneous linewidths of < 0.07 cm^{-1}, corresponding to a lower limit of the lifetime ≈ 0.1 ns. Given that both electron and optical spectroscopies agree that these states are all above the $O(^3P) + O_2(^3\Sigma_g^-)$ dissociation asymptote and the long radiative lifetime, a direct study of the stability and dissociation dynamics was in order.

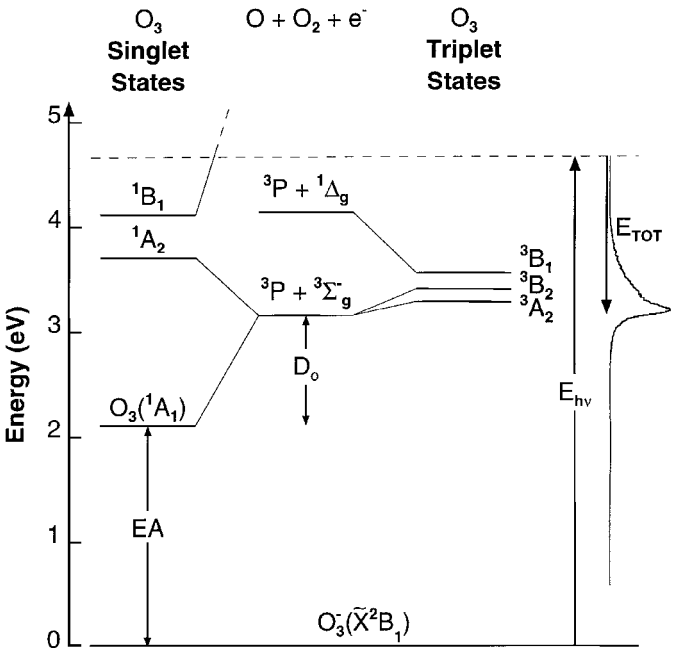

Figure 9. Energy level diagram for O_3^- and O_3, showing the total translational energy release spectrum ($E_{TOT} = E_T + eKE$). The electronic states are labelled in C_{2v} symmetry and the energetics are defined in the text. The adiabatic correlations between states and photoproducts are also shown. The ordering of the excited states is from Arnold *et al.* [71].

4.1. *Photoelectron spectra of excited states of O_3*

To address the question of the stability of the low-lying excited states of O_3, the simplest measurement involves an examination of the 266 nm (4.66 eV) photoelectron spectra of O_3^- in coincidence with O_3 and/or $O + O_2$ photofragments. If the lifetime of the excited states is longer than the flight time from the interaction region to the photofragment detector, stable O_3 should be observed in coincidence with photoelectrons corresponding to production of the excited states of O_3. In these measurements the detector was placed off-centre, so both O_3 and O or O_2 photofragments could be observed. In figure 10(A) the *eKE* spectrum coincident with either O_3 or one of the photofragments is shown. The signal observed in this spectrum in the range 1.7 eV $<$ *eKE* $<$ 3.0 eV corresponds to production of ground state O_3 ($\tilde{X}^1A_1$). The figure also shows a Franck–Condon simulation of the $^3A_2$ ($v_2' = 0, 1$) and $^3B_2$ ($v_2' = 0$) excited state region of the spectrum, *eKE* $\approx$ 1.1–1.5 eV. This simulation, adapted from the results of Arnold *et al.* [71] assumes a 450 K vibrational temperature of the anion to account for the hot bands evident at $\approx$ 1.4 eV. The simulation is seen to fit the leading edge of the excited state photoelectron signal, and can be used as an indication of the expected signature of stable excited states. The photoelectron spectrum of the *stable* states of O_3 is shown in figure 10(B). Stable O_3 is identified by the arrival at the photofragment detector of a single particle at the beam velocity in coincidence with a photoelectron. Also shown in this frame is the Franck–Condon fit for the $^3A_2$ ($v_2' = 0, 1$) states. No evidence of stable O_3 is observed in the $^3A_2$ region other than false coincidence background. Thus, while $O_3(\tilde{X}^1A_1)$ is stable, the excited states dissociate faster than the 6 μs flight time to the detector at a beam energy of

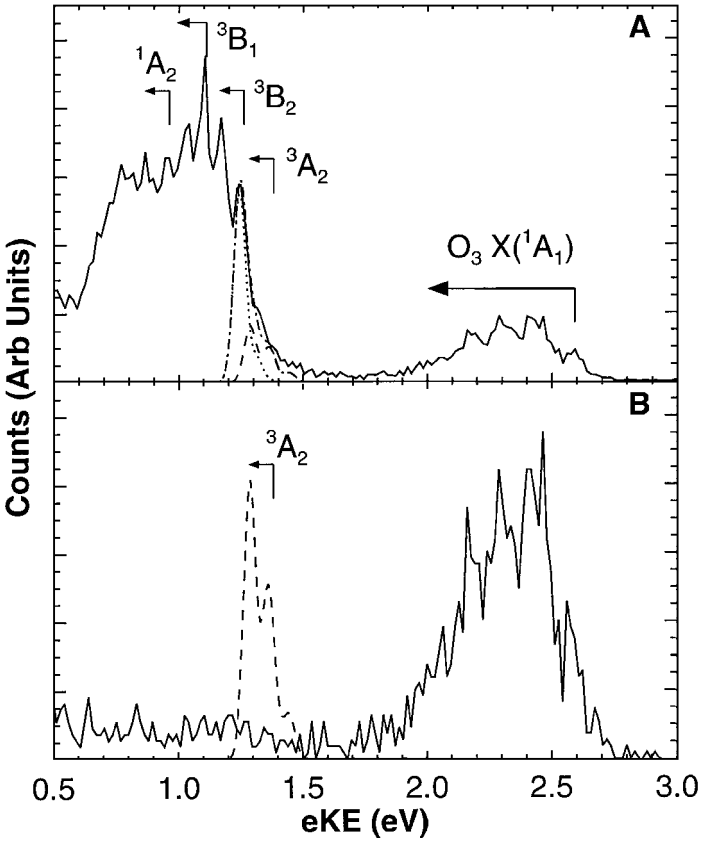

Figure 10. 266 nm photoelectron spectra of O_3^- with the photofragment detector beam-block removed. The laser polarization was parallel to the ion beam. Frame (A) includes contributions from both stable and dissociating O_3. Frame (B) includes contributions from only stable O_3 and false coincidences. Dashed curves are Franck–Condon fits (see text for details).

6 keV. A further test involved comparisons of the photofragment translational energy release spectra at beam energies of 2.5 and 4.0 keV. If the excited state lifetime was greater than 0.5 μs, the apparent E_T would be reduced at the higher beam energy. The consistency of the measurements at these two beam energies showed that the dissociation is prompt.

The spectrum in figure 10(A) is consistent with the high-resolution photoelectron study of Arnold *et al.* [71]. The peaks at high *eKE*, spaced by 70–80 meV, were assigned by Arnold *et al.* to overlapping bending vibrations in the three lowest triplet states, $^3A_2$, $^3B_2$, and $^3B_1$ as shown. Studies of the polarization dependence of the spectra showed further resolved structure in the 0.5–1.4 eV range, allowing a tentative assignment of the origin of the $^1A_2$ state as well [71].

4.2. *Photoelectron–photofragment energy correlations*

To examine the dissociation dynamics of the low-lying excited states of O_3, photoelectron–photofragment coincidence experiments were performed. The observation of resolved vibrational structure in the photoelectron spectra indicated that the dissociative states of O_3 survive for several vibrational periods so it appeared likely

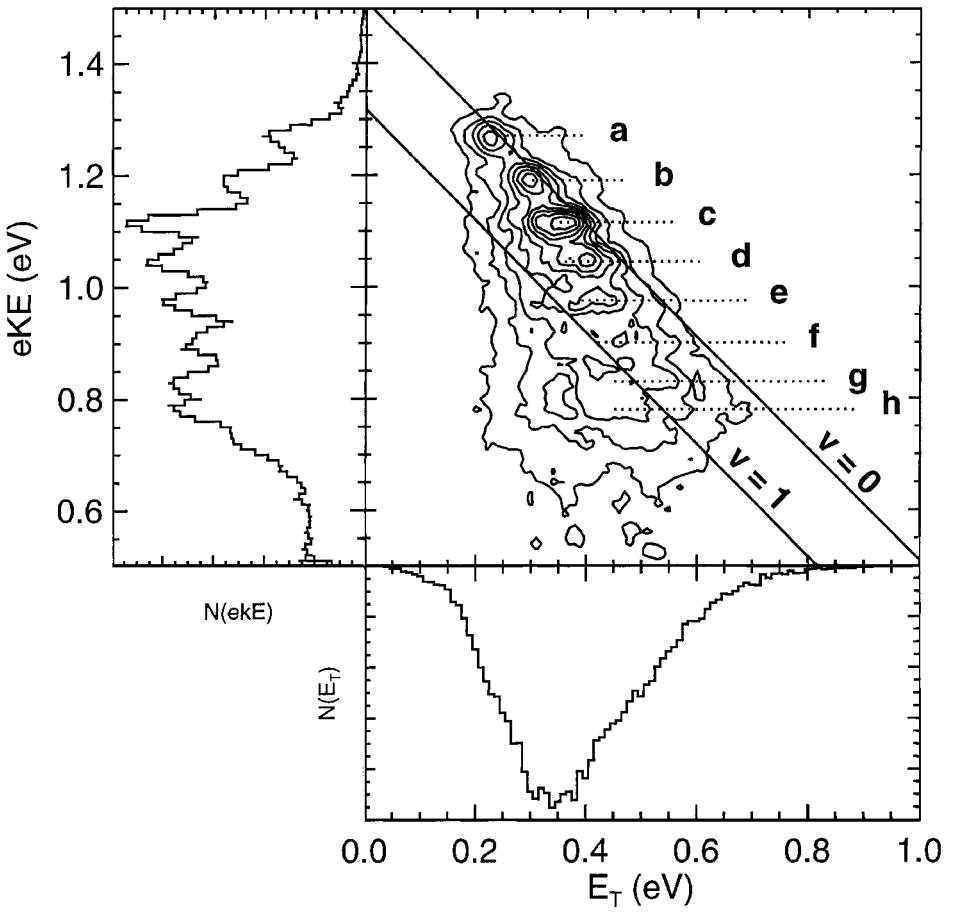

Figure 11. The $N(E_T, eKE)$ correlation spectrum for the DPD of O_3^-. Energetic thresholds for $[O(^3P)+O_2(^3\Sigma_g^-,\ v=0)+e^-]$ and $[O(^3P)+O_2(^3\Sigma_g^-,\ v=1)+e^-]$ are also shown. This spectrum was recorded with the laser polarization perpendicular to the ion beam. The E_T and eKE spectra shown along the x and y axes respectively. The photoelectron kinetic energy axis is truncated at 0.5 eV as no significant features are observed in the correlation spectrum below that energy.

that this would be an example of a sequential DPD process. Figure 11 shows the $N(E_T, eKE)$ correlation spectrum for O_3^-, comprising $\approx$ 40 000 events. The two diagonal lines on the contour map represent the maximum translational energy for the production of ground state photofragments $[O(^3P)+O_2(^3\Sigma_g^-, v=0)+e^-]$ and photofragments with one quantum of vibration in O_2 $[O(^3P)+O_2(^3\Sigma_g^-, v=1)+e^-]$. These thresholds are determined from the photon energy (4.66 eV), the electron affinity of O_3 (EA = 2.103 eV) [69], the O–O_2 bond dissociation energy (D_o = 1.05 eV) [85], and the O_2 ($^3\Sigma_g^-$) vibrational quantum (ΔE = 0.193 eV). The estimated uncertainty in the $N(E_T, eKE)$ peak positions is $\pm$ 0.03 eV. The contours extend over the maximum translational energy limit for $v=0$, indicating some production of internally excited (vibrational and/or electronic) O_3^- in the ion source [86].

There are several prominent features evident in the contours of the correlation spectrum. The peaks labelled a–d in figure 11, appearing at highest eKE, correspond to the lowest levels of the excited states of O_3, and are arrayed along the translational

energy limit corresponding to ground state products. Thus, nearly all the available energy is appearing in translation with very little vibrational or rotational energy for these dissociation events. As eKE drops, and the excitation in O_3 increases, the features move away from the maximum translational energy, finally becoming the broad bands corresponding to peaks e–h in the photoelectron spectra. This shows that photofragments produced in coincidence with lower electron kinetic energies (the $^3B_1$ and $^1A_2$ states) yield products with a broader distribution of rotational and/or vibrational excitation.

The energy level diagram in figure 9 shows the adiabatic correlations between the excited states and the dissociation channels [75]. In addition, the total translational energy release spectrum ($E_{TOT} = eKE + E_T$) is shown vertically on the right-hand side of figure 9. $E_{TOT} = 0$ corresponds to no photodetachment and no photodissociation, which would leave the system at the photon energy. Increasing E_{TOT} corresponds to DPD to lower energy product states. It is interesting to note that in comparison to the highly structured E_{TOT} spectrum observed in the case of O_4^-, there is little structure evident in this spectrum. The E_{TOT} spectrum shows that DPD of O_3^- yields only ground electronic state products [$O(^3P) + O_2(^3\Sigma_g^-) + e^-$]. In the case of the $^1A_2$, $^3A_2$ and $^3B_2$ states this is not surprising, as they adiabatically correlate with the observed ground state products. The $^3B_1$ state, however, correlates to [$O(^3P) + O_2(^1\Delta_g)$] and is well below this dissociation asymptote. Dissociation of the $^3B_1$ state to ground state products must therefore occur by a non-adiabatic interaction.

4.3. *Excited state lifetimes and dynamics of O_3*

The results presented here show that the low-lying excited states of O_3 dissociate promptly, with an upper limit to the dissociation lifetime of 0.5 μs. An important question concerns how these measurements compare to the recent work of Bouvier *et al.* [77] Rovibronic fine structure observed in their experiment indicates the presence of a barrier to dissociation of the two lowest bending vibrations of the $^3A_2$ state [63, 77]. The small difference in equilibrium bond angles between the ground state neutral (116.6°) and the anion (115.5°) [78] indicates that photodetachment and optical excitation should access similar Franck–Condon regions in the bending coordinate of the excited states. The Franck–Condon region in the symmetric stretch is quite different, however, due to the fact that the O–O bond length of the ground state anion (1.376 Å) is similar to the calculated value of the $^3A_2$ state (1.369 Å), while the ground state neutral has a much shorter bond length of 1.291 Å [78]. Therefore the photoelectron spectra are dominated by bending excitation, while optical absorption should produce both bend and stretch excitation. The O_3^- produced by electron-impact in a pulsed supersonic jet is expected to have rotational temperatures of the order of 50 K [31], so it is anticipated that photodetachment will primarily produce low rotational levels in the $^3A_2$ state. Thus, it is expected that photodetachment of O_3^- should effectively populate the $^3A_2$ levels observed by Bouvier *et al.* [77]. In conjunction with the linewidths observed by Bouvier *et al.*, our results indicate a range of 0.1 to 500 ns for the lifetime of the $v_2 = 0$, 1 levels of the $^3A_2$ state.

The $N(E_T, eKE)$ correlation spectra show that dissociation of the two lowest triplet states ($^3A_2$ and $^3B_2$) leads to virtually all the available energy appearing in translation. For the $^3B_1$ and $^1A_2$ states, considerably more energy appears in rotation and/or vibration of the O_2 product. The results also indicate that the $^3B_1$ state dissociates non-adiabatically to ground electronic state products.

Dissociation of the low-lying excited states of O_3 is likely to proceed by distortion

from C_{2v} to C_s symmetry along the asymmetric stretch coordinate. An alternative mechanism, involving elimination of the central O atom and preserving C_{2v} symmetry may also be considered. [69] Elimination of the central O atom would be expected to produce significant vibrational excitation of the nascent O_2 fragment. The asymmetric dissociation mechanism, on the other hand, is expected to yield a large fraction of energy in translation along with some rotational and vibrational excitation, which is more consistent with the observed dynamics. In the low levels of the $^3A_2$ and $^3B_2$ states there is no evidence at all of vibrational excitation. As dissociation of the $^3B_1$ and $^1A_2$ states occurs, more energy appears in rotation and perhaps vibration as well. The absence of resolved O_2 vibrational states in the translational energy distribution indicates, however, that rotational excitation in excess of the vibrational spacing of O_2 occurs in this energy range. These results are most consistent with the asymmetric dissociation pathway.

Levene and Valentini discussed the photodissociation dynamics of O_3 in the Huggins band in terms of a modified impulse model, in which the partitioning of energy between translation and rotation is determined by the impulse along the breaking bond [87]. In this model, impulsive vibrational excitation is ignored and the product vibrational distribution was found to be approximated by a Franck–Condon distribution between the excited state of O_3 and the product O_2. These dynamics may provide a qualitative explanation of the product translational energy distribution for dissociation of the $^1A_2$ and $^3B_1$ states (peaks d–h in the $N(E_T, eKE)$ correlation spectra of figure 11).

The modified impulse model fails to describe dissociation of the low levels of the $^3A_2$ and $^3B_2$ states. Peaks a–c in figure 11, assigned to these states, exhibit no product vibrational and little rotational excitation. This model predicts 0.06 eV in rotation for peak a if one uses the equilibrium bond angle of the $^3A_2$ state of 99.2° [78]. This is significantly larger than the nominal observed value of 0.01 eV. The impulse model can, of course, still work if it is arbitrarily assumed that in the excited state the molecule distorts into a more linear configuration before the bond breaks impulsively. A factor which may contribute to the breakdown of the impulse approximation is the small available energy in dissociation of the $^3A_2$ and $^3B_2$ states. The small repulsion between the products provides greater opportunity for exit channel interactions, contrary to the fundamental assumption of a sudden impulse. As Schinke pointed out, the details of the bending potential and exit channel interactions can play a crucial role in rotational excitation [88]. As more detailed potential energy surfaces for the low-lying states of O_3 become available, it should be possible to carry out realistic dynamics calculations to compare with the present experiments.

The non-adiabatic dissociation of the $^3B_1$ state further confirms that the excited state dynamics of O_3 are complicated and it is also consistent with the asymmetric dissociation pathway. Theoretical studies have shown that both singlet and triplet conical intersections occur in C_s symmetry involving the $^1B_1$, $^1A_2$ and $^3B_1$, $^3A_2$ states respectively [78, 80]. Thus, it is most likely that dissociation of the $^3B_1$ state to ground state products occurs through this interaction with the lower $^3A_2$ state. The singlet state conical intersection has been previously invoked by Braunstein *et al.* [80] to explain the observation by Levene *et al.* [64] of only ground state $O(^3P) + O_2(^3\Sigma_g^-)$ products after excitation to the $^1B_1$ state. In that case, the $^1B_1$ state is known to adiabatically correlate to higher energy $O(^1D) + O_2(^1\Delta_g)$ products. In a similar fashion, dissociation of the $^3B_1$ state to ground state products can occur after a crossing to the $^3A_2$ surface.

In C_{2v} symmetry the $^3A_2$ and $^3B_1$ states cross, however, they become the two lowest $^3A''$ states in C_s symmetry, forming the conical intersection [80]. As dissociation begins along the asymmetric stretch coordinate, the molecular symmetry drops to C_s and the molecule may find itself on the lower dissociative surface. The calculated geometries of the anion and the neutral excited states shows that $O_3^-(\tilde{X}\,^2B_1)$ has a bond angle of 115.5° while the $^3A_2$ and $^3B_1$ states of O_3 have bond angles of 99.2° and 123.7° respectively [78]. The large difference in bond angles between O_3^- and the O_3 $^3B_1$ state is expected to yield significant bending excitation upon photodetachment. This bending excitation may promote sampling of the conical intersection leading to facile dissociation of the $^3B_1$ state to ground state photoproducts via the intermediate $^3A_2$ state. It is interesting to note that peak c in the correlation spectra, assigned to the $^3B_1$ state by Arnold *et al.* [71], marks the beginning of the trend to greater rotational excitation in the O_2 products. This may be a direct signature of the non-adiabatic interaction, and should provide an important test of future theoretical models of this dissociation.

5. Dissociative photodetachment of isomeric anions: $NO^-(N_2O)$ and $N_3O_2^-$

To assess the role played by isomeric forms of molecular and cluster ions in plasmas and other environments it is essential to characterize the energetics and structures of potential isomers. A variety of experimental techniques including optical and photoelectron spectroscopies [89], photodissociation and collision-induced dissociation [90, 91] and cluster reactivity studies [92] have previously been used to infer the properties of molecular and cluster anions. In this third example of DPD dynamics, the application of photoelectron–photofragment coincidence spectroscopy to the characterization of isomeric forms of the $N_3O_2^-$ molecular ion are reviewed.

Recent photodetachment experiments and high-pressure mass spectrometry studies have stimulated interest in isomeric forms of $N_3O_2^-$. Using photoelectron spectroscopy, Coe *et al.* [93] observed spectra consistent with an ion–dipole complex $NO^-(N_2O)$. The spectrum they recorded at 514 nm (2.54 eV) is similar to the photoelectron spectrum of free NO^- showing a long vibrational progression in the neutral NO. The spectrum showed a shift to a higher electron binding energy of ≈ 0.22 eV. These results were interpreted as resulting from an intact NO^- core ion solvated and stabilized by N_2O. The shift in the electron affinity is primarily due to the ion-induced-dipole interaction in the anion.

Hiraoka and co-workers used high-pressure mass spectrometry to examine the equilibria of ion–molecule reactions in N_2O and found evidence for a more stable isomer $N_3O_2^-$ [94]. Given the abundance of $N_3O_2^-$ in their room-temperature ion source, they suggested a binding energy of this species of at least ≈ 0.4 eV, raising the possibility that a covalently bound molecular anion, $N_3O_2^-$, exists. Hiraoka *et al.* [94] could not obtain quantitative experimental data on the stability of $N_3O_2^-$ but performed *ab initio* calculations (MP2/6-31+G*//ROHF/6-31+G) which indicated the presence of both a covalently bound W-shaped $O–N–N–N–O^-$ molecule and the ion–dipole complex $NO^-(N_2O)$. These calculations showed that the covalent $N_3O_2^-$ is stabilized by ≈ 1.25 eV relative to $NO + N_2O + e^-$.

In these experiments photoelectron and photofragment kinetic energies were measured in coincidence to fully characterize the process $N_3O_2^- \rightarrow NO + N_2O + e^-$. In the DPD of $N_3O_2^-$, two pathways were observed, one leading to a large translational energy release and an unstructured photoelectron spectrum, and the other leading to a small translational energy release and a structured photoelectron spectrum. These

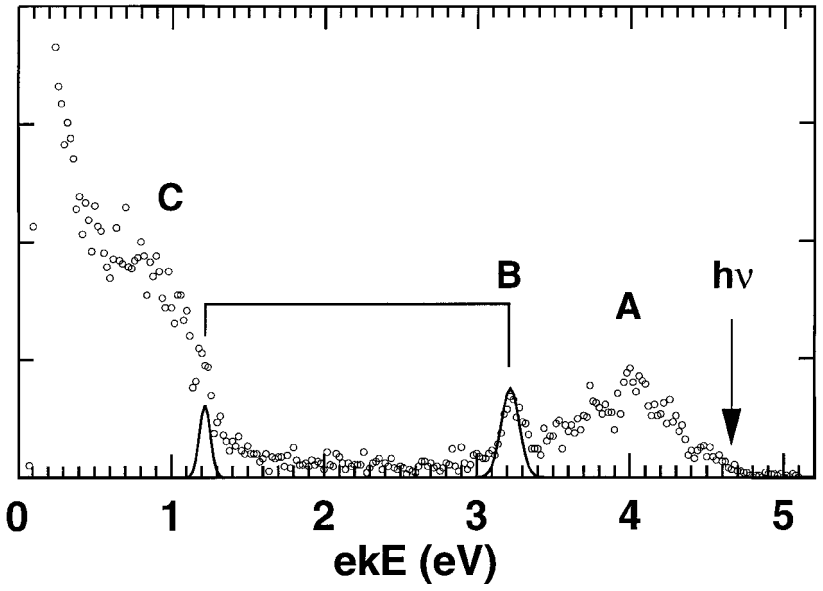

Figure 12. 266 nm photoelectron spectrum of $N_3O_2^-$. These data were recorded with the laser polarization parallel to the ion beam at an energy of 6 keV. The features labelled A, B and C in the 266 nm data are discussed in the text.

results show that two isomeric forms of $N_3O_2^-$ are formed by electron impact on N_2O in a free-jet expansion: an ion–dipole complex, $NO^-(N_2O)$, and a more stable molecular anion, $N_3O_2^-$.

5.1. *Photoelectron spectra and photofragment translational energy distributions*

Photoelectron spectroscopy provides clear evidence for two forms of this anion. The photoelectron spectra at 532 and 355 nm exhibit structure similar to that reported by Coe *et al.* [93] at 514 nm. A vibrational progression resembling that observed for free NO^- [95], with NO^- to NO vibrational transitions from $v'' = (0)$ to $v' = (0–5)$, was observed with an apparent photodetachment onset at an electron binding energy of 0.25 eV. This is a shift of 0.22 eV to higher electron binding energy relative to free NO. There is little change in the overall Franck–Condon profile but some broadening occurs for the individual transitions. As discussed by Coe *et al.* [93], these photoelectron spectra are consistent with a weakly bound cluster ion $NO^-(N_2O)$, i.e. a solvated NO^- core.

Increasing the photon energy to 4.66 eV, however, reveals new features in the photoelectron spectrum as shown in figure 12. In addition to the characteristic $NO^-(N_2O)$ signal at high electron kinetic energies (A), there are two new features—a large broad shoulder at ≈ 0.9 eV (C), and a sharp peak and a shoulder (B). The $NO^-(N_2O)$ feature (A) shows no vibrational resolution at this wavelength due to the decrease in resolution of the TOF measurement for these high-energy photoelectrons. The features B at 3.2 and 1.2 eV arise from photodetachment of $O^- + h\nu \rightarrow O(^3P)$, $O(^1D) + e^-$. This implies that O^- is produced by photon absorption at 266 nm. All *eKE* spectra show a peak at low energy (0.12 eV) which results from stray laser- and ion-beam-induced photoelectrons. This background signal peaks at low energy and falls off rapidly with small contributions to the spectra beyond 0.5 eV.

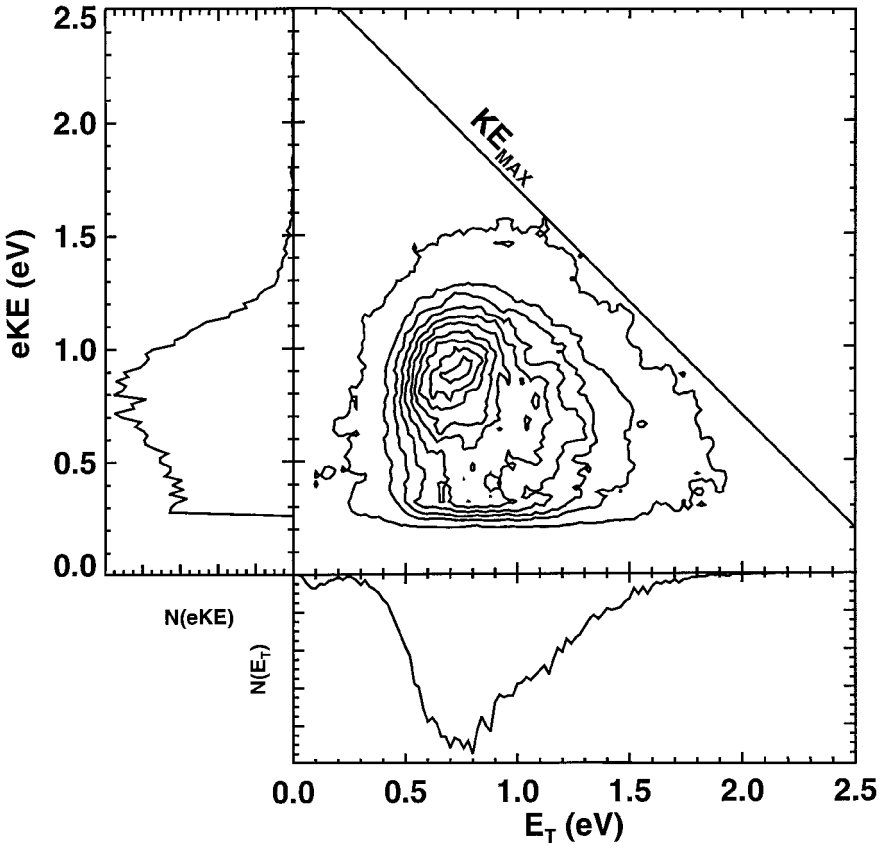

Figure 13. Correlation spectrum of the photoelectron kinetic energy with the photofragment translational energy release at 266 nm, recorded at a beam energy of 4 keV with the laser polarization parallel to the beam velocity. 19000 triple-coincidence events are included in this two-dimensional histogram and smoothed with a five-point boxcar algorithm. The assigned maximum kinetic energy for the photoelectron+photofragments, KE_{MAX} = 2.7 eV, is shown as the solid diagonal line. The lowest contour, near KE_{MAX}, is at 2% of the peak, with the rest of the contours linearly spaced from 15% to 95%.

Photofragment translational energy release spectra, $N(E_T)$, were recorded at all three wavelengths, showing a two-component spectrum. A large feature rising at $E_T < 0.1$ eV shows that most neutrals dissociate with very little recoil. Photoelectron–photofragment correlation spectra show that this low-E_T feature is coincident with photoelectrons from the ion–dipole $NO^-(N_2O)$ complex. At all recoil energies, the photofragment mass spectrum peaks at 30 (NO) and 44 (N_2O) amu, with a FWHM of $\pm$ 1 amu at $E_T > 0.3$ eV. The ability to determine the photofragment mass ratio from time and position measurements decreases as the photofragment recoil decreases at low E_T. At low E_T, however, the only plausible products are $NO + N_2O$ from dissociation of the weakly perturbed $NO(N_2O)$ complex produced by photodetachment of the ion–dipole complex $NO^-(N_2O)$.

The high-E_T peak in the spectra is observed at 0.7–0.9 eV at all three wavelengths. This channel is enhanced by a factor of $\approx$ 500 as the photon energy is increased from 2.33 to 4.66 eV. The presence of the high-E_T channel shows that $NO + N_2O$ photofragments are produced at all wavelengths with significant repulsion in the

nascent neutral complex. The qualitative conclusion that can be reached from these data is that photodetachment or photodissociation followed by autodetachment produces neutral species with both low and high repulsion at all wavelengths.

5.2. $N(E_T, eKE)$ *correlation spectra*

The $N(E_T, eKE)$ correlation spectrum yields both a measure of the overall DPD dynamics and the stability of the ion relative to the free electron and photofragments. High signal-to-noise correlation spectra showing the origin of the high-E_T channel at 532 and 355 nm were not obtained due to the small cross section for the high-E_T channel at these wavelengths. Spectra recorded at 532 nm clearly showed the correlation of the $NO^-(N_2O)$ photoelectrons with the low-E_T channel. The correlation spectrum at 266 nm is shown as the contour map in figure 13. The contour map shows that the broad photoelectron peak observed at 0.9 eV in the $N(eKE)$ spectrum is correlated with the high-E_T peak in the $N(E_T)$ spectrum, indicating that photodetachment of $N_3O_2^-$ accesses a region of the $NO + N_2O$ neutral surface which is characterized by a significant repulsion and hence a large translational energy release.

While the photoelectron spectrum yields the vertical detachment energy directly, the $N(E_T, eKE)$ correlation spectrum yields an estimate of the stability of covalently bound $N_3O_2^-$ relative to $NO + N_2O + e^-$. The total available energy is defined as the difference between the photon energy and the energy required to produce $NO + N_2O + e^-$ at zero translational energy and in the lowest quantum states. Energy conservation dictates that DPD events are constrained to lie within a triangle formed by the eKE and E_T axes and the maximum kinetic energy of the three particles, KE_{MAX}. The lowest contours in figure 13 display the triangular shape dictated by energy conservation. The diagonal line drawn at the 2% contour in figure 13 from $(E_T, eKE) = (0.0, 2.7)$ to (2.7, 0.0) provides an estimate of KE_{MAX}. Given the photon energy of 4.66 eV, this indicates that $N_3O_2^-$ is stabilized relative to $NO + N_2O + e^-$ by 2.0 eV. This is an accurate measure of the stability if it is assumed that some of the $NO + N_2O$ products are produced with no internal excitation, and the parent $N_3O_2^-$ is cold. The latter assumption is reasonable given that this ion source also produces the weakly bound $NO^-(N_2O)$ ion. Since both NO and N_2O are likely to be produced with vibrational and rotational excitation, however, this must be taken as an upper limit on the stability, i.e. the stabilization of $N_3O_2^-$ may be less than 2.0 eV relative to $NO + N_2O + e^-$, as discussed below.

5.3. *Dissociative photodetachment dynamics*

When a strongly bound anion has Franck–Condon overlap only with a highly repulsive region of a neutral potential energy surface, both the photoelectron and photofragment translational energy release must be measured in coincidence to obtain a value for the stability of the anion relative to a free electron and the neutral products. However, consideration of either the $N(eKE)$ or $N(E_T)$ spectra alone provides evidence for the existence of at least two isomeric forms of $N_3O_2^-$. The $N(eKE)$ spectra at 532 and 355 nm support the solvated NO^- interpretation given by Coe *et al.* [93] $NO^-(N_2O)$ is a weakly bound ion–dipole complex where the excess charge resides largely on the NO. The resulting photoelectron spectra closely parallel that of free NO, with a stabilization of 0.22 eV upon solvation. The observation of the broad photoelectron signal at 266 nm (C in figure 12) is indicative of a different form of the anion. The occurrence of other photodestruction processes is also shown by the observation of the O^- photoelectron spectrum at 266 nm.

Translational spectroscopy provides a measure of the repulsion in the nascent neutral. Consider photodetachment of the ion–dipole complex $NO^-(N_2O)$. Given the small solvation energy in the cluster, little nuclear rearrangement and thus little repulsive energy is expected in the photodetached neutral complex. In this case, the energy released in translation between the $NO + N_2O$ photofragments is expected to be small, consistent with the significant low-E_T channel observed at all wavelengths. A high-E_T channel is also observed at all wavelengths, although it is very weak at 532 and 355 nm. This indicates that a fraction of the $NO + N_2O$ molecules are produced with significant repulsive energy.

The broad photoelectron peak at $eKE = 0.9$ eV is shown to be correlated with the high-E_T channel at 266 nm in the $N(E_T, eKE)$ correlation spectrum, providing strong evidence for the covalent $N_3O_2^-$ anion. The absence of extensive structure in the eKE spectrum could be a result of transitions between low-frequency vibrational modes in the anion and the neutral. Given that the photoelectrons are observed to be correlated with the high-E_T channel, however, the simplest explanation for this feature is direct DPD on a repulsive surface. An alternative explanation is that photodissociation producing vibrationally excited $NO^- + N_2O$ occurs, followed by rapid autodetachment of the $NO^-(v > 0)$ [96]. Unless autodetachment occurs so rapidly that the NO^- is substantially perturbed by the recoiling N_2O molecule, observation of autodetachment structure in the photoelectron spectrum would be expected.

The data obtained on the stability of the covalent form, $N_3O_2^-$, in these experiments are summarized in figure 14. The covalent form, $N_3O_2^-$, is placed at -2.0 eV relative to the $NO + N_2O + e^-$ dissociation asymptote. The photon energies for 355 and 266 nm photodetachment are plotted relative to the $N_3O_2^-$ origin. The E_T spectrum at 266 nm provides a measure of the photofragment repulsion, and is plotted with $E_T = 0$ at the $NO + N_2O + e^-$ dissociation asymptote. The 266 nm photoelectron spectrum is plotted as the photoelectron binding energy, $E_{bind} = E_{h\nu} - eKE$, directly showing the vertical excitation required to reach the repulsive state of N_3O_2 from $N_3O_2^-$. The intensity distribution in the 266 nm photoelectron spectrum shows that Franck–Condon overlap with the repulsive state of N_3O_2 is greatest at ≈ 1.9 eV above $NO + N_2O + e^-$. The signal in the 266 nm photoelectron spectrum extends below the 355 nm photon energy, indicating that the repulsive state can also be accessed by photodetachment at 355 nm. This explains the increased intensity in the high-E_T channel at 355 nm relative to 532 nm. DPD of $N_3O_2^-$ at 532 nm is not energetically accessible, however, indicating that the weak high-E_T channel at that wavelength has a different origin. The 266 nm total translational energy release spectrum, obtained by binning $E_{TOT} = eKE + E_T$ for each coincident event, is shown plotted with $E_{TOT} = 0$ at the 266 nm photon energy. This shows that the coincidence data are consistent with the DPD of $N_3O_2^-$: $N_3O_2^- \rightarrow NO + N_2O + e^-$.

As discussed above, the correlation spectrum allows determination of a 2.0 eV upper limit to the stability of $N_3O_2^-$ relative to $NO + N_2O + e^-$. For this to be an accurate measure of the stability requires two conditions—cold $N_3O_2^-$ and production of at least some ground state $NO + N_2O$ products. Significant internal excitation in the photoproducts is expected, however. Hiraoka's most stable calculated geometry for the covalent $N_3O_2^-$ finds the N_2O moiety to be bent by 115.5°. When this isomer dissociates, N_2O will become linear resulting in a photoproduct with substantial excitation in the bending mode at ≈ 590 cm^{-1}, in addition to other internal degrees of freedom in NO and N_2O. Examination of the E_{TOT} spectrum in figure 14 shows some signal extending ≈ 0.2 eV below $NO + N_2O + e^-$. If it is assumed that none of this is

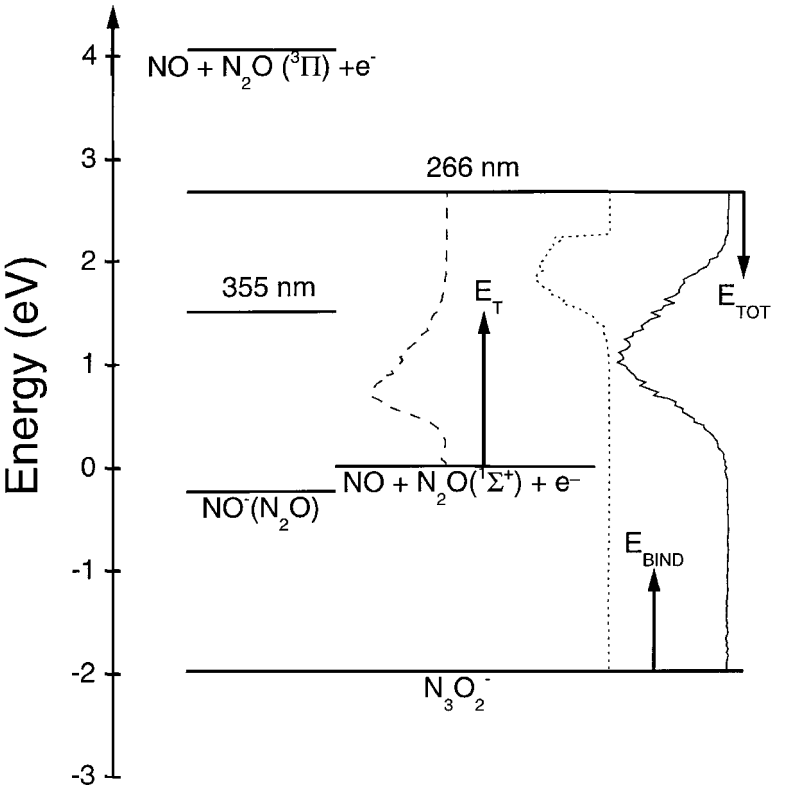

Figure 14. Energetics of the DPD of $N_3O_2^-$. $NO + N_2O + e^-$ is shown as the zero of energy. $NO^-(N_2O)$ is shown at -0.24 eV [93], and the covalent isomer $N_3O_2^-$ is shown at -2.0 eV. The vertical long-dashed spectrum shows $N(E_T)$ at 266 nm, plotted with $E_T = 0$ at the $NO + N_2O + e^-$ asymptote. The vertical short-dashed spectrum shows the photoelectron spectrum at 266 nm, plotted as electron binding energy relative to $N_3O_2^-$. Finally the vertical solid spectrum shows the total translational energy spectrum, $N(E_{TOT})$, at 266 nm, plotted with $E_{TOT} = 0$ at the photon energy.

due to vibrational excitation in the anion, the stability of $N_3O_2^-$ would have to be decreased to 1.8 eV relative to $NO + N_2O + e^-$. Similarly, if no ground state fragments are produced, no signal is observed at the true maximum E_{TOT}. This would also require a decrease in the stability of $N_3O_2^-$. If vibrational excitation in excess of 0.2 eV in the anion appears in product (electron or photofragment) kinetic energy, an increase in the stability of $N_3O_2^-$ would be required. Due to these uncertainties, the stability of $N_3O_2^-$ is reported as 2.0 eV, with an estimated error of $\pm$ 0.2 eV.

An unexplained aspect of the DPD of $N_3O_2^-$ is the weak high-E_T channel observed at 532 nm. There are several possible explanations for this process. One involves vibrational to translational energy transfer in the $NO(v)$–N_2O neutral complex. To peak at 0.7 eV, transfer of three vibrational quanta to translation would need to be the dominant process, which appears unlikely to be the case at the relatively low vibrational excitation of NO ($v \leqslant 6$) produced in photodetachment [97]. A second possibility is a third isomer, with the charge localized on the N_2O. Based on the adiabatic electron affinity of N_2O (0.22 eV) [98], the N_2O^-(NO) species is expected to be more stable than $NO^-(N_2O)$, but more difficult to form since a substantial barrier to electron attachment exists. N_2O is linear, but N_2O^- is expected to be bent by

approximately 134° [99]. The energy required to bend the neutral 134° is estimated to be 1 eV, presenting a substantial barrier to localization of the electron on N_2O which may channel into photofragment translation upon photodetachment of an N_2O^-(NO) isomer. Because of the large geometry difference between N_2O and N_2O^-, there is poor Franck–Condon overlap between the lowest energy levels in the ion and neutral, and any photoelectrons produced in photodetachment of N_2O^-(NO) would be expected to be distributed over a broad energy range, as observed by Coe *et al.* in N_2O^- and $(N_2O)_2^-$ [100]. This would make observation of this isomer in the photoelectron spectra difficult, so it cannot be ruled out.

Another aspect of the photochemistry of $N_3O_2^-$ which needs further characterization is the observation of O^- production at 266 nm. This indicates that ionic photodissociation also occurs for this system, however, no two-body photodissociation channels producing stable ionic products were identified. Free NO^- was not observed to photodissociate at this wavelength, so this observation indicates that another dissociation pathway exists. Considering the possible products of this photodissociation, the energetically most likely reaction is the three-body process: $N_3O_2^- + h\nu \rightarrow N_2 + NO + O^-$. This reaction has been previously discussed as a source of O^- from the reaction $NO^- + N_2O$ by Gorden and Ausloos [101]. Whether this reaction occurs on a repulsive ionic surface or perhaps via photo-assisted dissociative electron attachment (DEA) to N_2O [102] remains to be determined. Photo-assisted DEA might occur in the ion–dipole complex when the electron photodetached from NO attaches to the nearby N_2O molecule, leading to the well-known dissociative attachment reaction $N_2O + e^- \rightarrow N_2 + O^-$. It is unclear, however, why this channel would only be observed at 266 nm as the cross section for dissociative attachment to free N_2O peaks at an electron energy of 2.5 eV [103]. Photodetached electrons at an energy of $\approx$ 2.5 eV are most efficiently produced at 355 nm, where no evidence for the O^- channel has been observed. It is possible, however, that the nearby NO may affect the energy dependence of the dissociative attachment cross section.

Papai and Stirling have recently performed density functional calculations on the stability of covalently bound neutral N_3O_2 species [104]. They found both cyclic and open, 'W-type', isomers, with the cyclic isomer being more stable. However, while both isomers appear to have stable local minima, they are energetically unstable relative to $NO + N_2O$ or $N_2 + NO_2$. According to the calculations of Hiraoka *et al.* [94], the W-type isomer is the most stable form of the anion. Papai and Stirling noted that this isomer of the neutral is destabilized by 0.13–0.35 eV relative to cyclic N_3O_2. The W-type isomer of neutral N_3O_2 was found to be $\approx$ 1 eV higher in energy than $NO + N_2O$, a result which is qualitatively consistent with the energetics deduced from the 266 nm photoelectron spectrum, which shows a peak in the photoelectron spectrum at $\approx$ 1.9 eV above $NO + N_2O$ as shown in figure 14. The observations reported here show no evidence for the production of stable N_3O_2 produced by photodetachment of $N_3O_2^-$, either due to a lack of Franck–Condon overlap with bound regions of the N_3O_2 potential energy surface or the absence of long-lived states of N_3O_2.

These studies show that there are at least two forms of $N_3O_2^-$ produced in the electron impact free-jet ion source: the ion–dipole complex and a more stable molecular anion. DPD of the ion–dipole complex is observed to lead to low translational energy release. DPD of the covalently bound complex, however, leads to a translational energy release peaking at $E_T \approx 0.8$ eV. Coincidence measurements of photoelectron and photofragment kinetic energies in DPD provide an experimental upper limit of 2.0 eV for the stability of $N_3O_2^-$. These observations provide an example

of the role photoelectron–photofragment coincidence spectroscopy can play in assessing the structure, energetics and dynamics of isomeric molecular and cluster anions.

6. Concluding remarks

An obvious direction for future photoelectron–photofragment coincidence experiments is the study of the dynamics of the transition state for fundamental reactions previously studied by photoelectron spectroscopy [4]. The transition state spectroscopy experiments carried out to date yield information on the neutral potential energy surface for bimolecular reactions near the transition state by analysis of the photoelectron spectra of bound anion precursors. Photoelectron–photofragment coincidence spectroscopy could extend these studies significantly by allowing detailed characterization of the entire DPD event. This would allow the earlier transition state spectroscopy experiments to be carried to their logical conclusion—preparation and energy analysis of the complex by measurement of the photoelectron energy and subsequent determination of the asymptotic properties of the photofragments produced by decay of the complex. Transition state spectroscopy experiments have provided the inspiration for numerous theoretical studies, providing a connection between the observed spectra, scattering dynamics and the potential energy surfaces for these fundamental reactions. Extending the earlier experiments via photoelectron–photofragment coincidence data will provide a valuable set of comparisons between theory and experiment, since recent theoretical studies have included detailed treatments of the dynamics of the photodetached electron [105, 106].

Another direction for photoelectron–photofragment coincidence experiments is the study of three-body dissociation dynamics. Photodetachment of a cluster precursor to a three-body reaction, with energy analysis of the photoelectron and photofragments in coincidence would provide a new level of detail concerning the dynamics of three-body dissociation reactions. We have built a second spectrometer with a multi-particle detector and have already carried out proof-of-principle experiments on the DPD of O_6^- at 532 nm: $O_6^- + h\nu \rightarrow O_2 + O_2 + O_2 + e^-$ [107]. These are timely experiments due to the increasing interest in three-body dissociation processes in neutral molecules [108].

The diverse dynamics encountered in DPD processes have been reviewed here, providing examples of both direct (O_4^-) and sequential (O_3^-) DPD dynamics. These examples show some of the unique insights to be gained from the study of DPD by the photoelectron–photofragment coincidence technique, including information on repulsive states of transient neutrals, molecular-frame photoelectron angular distributions, optically forbidden excited states, and the isomeric forms of polyatomic anions. Future improvements in lasers and particle detection techniques will allow extension of these experiments to a variety of new systems and problems.

Acknowledgments

I would like to acknowledge the contributions of my research group, including Dr. K. A. Hanold, C. R. Sherwood, M. C. Garner, Dr. M. S. Resat, Dr. V. Zengin, Dr. R.-J. Li, A. K. Luong and K. M. Strong, to these studies. R. E. C. is a Camille Dreyfus Teacher–Scholar, A. P. Sloan Research Fellow and a Packard Fellow in Science and Engineering. This work was supported by the NSF under grants CHE-937128 and CHE-9700142 and the US Air Force Office of Scientific Research, AFOSR-F49620-96-1-0220.

References

[1] Ervin, K. M., and Lineberger, W. C., 1992, *Advances in Gas Phase Ion Chemistry*, *Vol. 1*, edited by N. G. Adams and L. M. Babcock (Greenwich, CT: JAI Press) pp. 121–166.
[2] Arnold, S. T., Eaton, J. G., Patel-Misra, D., Sarkas, H. W., and Bowen, K. H., 1989, *Ion and Cluster Ion Spectroscopy and Structure*, edited by J. P. Maier (New York: Elsevier) pp. 417–472.
[3] Metz, R. B., Bradforth, S. E., and Neumark, D. M., 1992, *Adv. chem. Phys.*, **81**, 1.
[4] Neumark, D. M., 1993, *Acc. chem. Res.*, **26**, 33.
[5] Ervin, K. M., Ho, J., and Lineberger, W. C., 1989, *J. chem. Phys.*, **91**, 5974.
[6] Wodtke, A. M., and Lee, Y. T., 1987, *Molecular Photodissociation Dynamics*, edited by M. N. R. Ashfold and J. E. Baggott (London: Royal Society of Chemistry) pp. 31–60.
[7] Eland, J. H. D., 1979, *Electron Spectroscopy: Theory, Techniques and Applications*, *Vol. 3*, edited by C. R. Brundle and A. D. Baker (New York: Academic Press) pp. 231–303.
[8] Eland, J. H. D., 1991, *Vacuum Ultraviolet Photoionization and Photodissociation of Molecules and Clusters*, edited by C. Y. Ng (Singapore: World Scientific) pp. 297–343.
[9] Powis, I., 1992, *Chem. Phys. Lett.*, **189**, 473.
[10] Shigemasa, E., Adachi, J., Oura, M., and Yagishita, A., 1995, *Phys. Rev. Lett.*, **74**, 359.
[11] Tellinghuisen, J., 1985, *Photodissociation and Photoionization*, edited by K. P. Lawley (New York: John Wiley) pp. 299–369.
[12] Berry, R. S., 1980, *Adv. Electron. electron Phys.*, **51**, 137.
[13] Sherwood, C. R., Garner, M. C., Hanold, K. A., Strong, K. M., and Continetti, R. E., 1995, *J. chem. Phys.*, **102**, 6949.
[14] Hanold, K. A., Sherwood, C. R., and Continetti, R. E., 1995, *J. chem. Phys.*, **103**, 9876.
[15] Sherwood, C. R., Hanold, K. A., Garner, M. C., Strong, K. M., and Continetti, R. E., 1996, *J. chem. Phys.*, **105**, 10803.
[16] Hanold, K. A., Garner, M. C., and Continetti, R. E., 1996, *Phys. Rev. Lett.*, **77**, 3335.
[17] Sherwood, C. R., 1995, *Ph.D. Thesis*, University of California, San Diego.
[18] Resat, M. S., Zengin, V., Garner, M. C., and Continetti, R. E., 1997, *J. phys. Chem.*, (in the press).
[19] Garner, M. C., Hanold, K. A., Resat, M. S., and Continetti, R. E., 1997, *J. phys. Chem.*, **101**, 6577.
[20] Sherwood, C. R., and Continetti, R. E., 1996, *Chem. Phys. Lett.*, **258**, 171.
[21] Wolf, S., Sommerer, G., Rutz, S., Schreiber, E., Leisner, T., Wöste, L., and Berry, R. S., 1995, *Phys. Rev. Lett.*, **74**, 4177.
[22] Muller, A., Djuric, N., Dunn, G. H., and Belic, D. S., 1986, *Rev. sci. Instrum.*, **57**, 349.
[23] Cheshnovsky, O., Yang, S. H., Pettiette, C. L., Craycraft, M. J., and Smalley, R. E., 1987, *Rev. sci. Instrum.*, **58**, 2131.
[24] Bordas, C., Paulig, F., Helm, H., and Huestis, D. L., 1996, *Rev. sci. Instrum.*, **67**, 2257.
[25] Eppink, A. T. J. B., and Parker, D. H., 1997, *Rev. sci. Instrum.*, **68**, 3477.
[26] Hotop, H., and Lineberger, W. C., 1985, *J. Phys. Chem. Ref. Data*, **14**, 731.
[27] Trevor, D. J., Van Woerkom, L. D., and Freeman, R. R., 1989, *Rev. sci. Instrum.*, **60**, 1051.
[28] Hanold, K. A., Sherwood, C. R., Garner, M. C., and Continetti, R. E., 1995, *Rev. sci. Instrum.*, **66**, 5507.
[29] Johnson, M. A., Alexander, M. L., and Lineberger, W. C., 1984, *Chem. Phys. Lett.*, **112**, 285.
[30] Johnson, M. A., and Lineberger, W. C., 1988, *Techniques for the Study of Ion–Molecule Reactions*, edited by J. M. Farrar and W. H. Saunders (New York: John Wiley), pp. 591–635.
[31] Continetti, R. E., Cyr, D. R., Metz, R. B., and Neumark, D. M., 1991, *Chem. Phys. Lett.*, **182**, 406.
[32] Proch, D., and Trickl, T., 1989, *Rev. sci. Instrum.*, **60**, 713.
[33] Continetti, R. E., Cyr, D. R., and Neumark, D. M., 1992, *Rev. sci. Instrum.*, **63**, 1840.
[34] Bakker, J. M. B., 1973, *J. Phys.* E., **6**, 785; 1974, *ibid.*, **7**, 364.
[35] Gardner, L. D., Graff, M. M., and Kohl, J. L., 1986, *Rev. sci. Instrum.*, **57**, 177.
[36] Xie, X., and Simon, J. D., 1989, *Optics Commun.*, **69**, 303.
[37] Martin, C., Jelinsky, P., Lampton, M., Malina, R. F., and Anger, H. O., 1981, *Rev. sci. Instrum.*, **52**, 1067.

[38] Continetti, R. E., Cyr, D. R., Osborn, D. L., Leahy, D. J., and Neumark, D. M., 1993, *J. chem. Phys.*, **99**, 2616.
[39] DeBruijn, D. P., and Los, J., 1982, *Rev. sci. Instrum.*, **53**, 1020.
[40] Zare, R. N., 1972, *Molec. Photochem.*, **4**, 1.
[41] Yang, S.-C. and Bersohn, R., 1974, *J. chem. Phys.*, **61**, 4400.
[42] Cosby, P. C., Ling, J. H., Peterson, J. R., and Moseley, J. T., 1976, *J. chem. Phys.*, **65**, 5267; Smith, G. P., Lee, L. C., Cosby, P. C., Peterson, J. R., and Moseley, J. T., 1978, *J. chem. Phys.*, **68**, 3818.
[43] Lee, L. C. and Smith, G. P., 1979, *J. chem. Phys.*, **70**, 1727.
[44] DeLuca, M. J., Han, C. C., and Johnson, M. A., 1990, *J. chem. Phys.*, **93**, 268; Han, C.-C., and Johnson, M. A., 1992, *Chem. Phys. Lett.*, **189**, 460.
[45] Travers, M. J., Cowles, D. C., and Ellison, G. B., 1989, *Chem. Phys. Lett.*, **164**, 449.
[46] Hiraoka, K., 1988, *J. chem. Phys.*, **89**, 3190.
[47] Huber, K. P., and Herzberg, G., 1979, *Molecular Spectra and Molecular Structure IV* (New York: Van Nostrand).
[48] Chertihin, G. V., and Andrews, L., 1997, *J. chem. Phys.*, (in the press).
[49] Aquino, A., Walch, S. P., and Taylor, P. R., work in progress.
[50] Chandra, N., 1986, *Chem. Phys.*, **108**, 301.
[51] Cooper, J., and Zare, R. N., 1968, *J. chem. Phys.*, **48**, 942.
[52] Dill, D., 1976, *J. chem. Phys.*, **65**, 1130.
[53] Rudolph, H., and McKoy, V., 1989, *J. chem. Phys.*, **91**, 2235.
[54] Park, H. K., and Zare, R. N., 1996, *J. chem. Phys.*, **104**, 4554.
[55] Reid, K. L., and Powis, I., 1994, *J. chem. Phys.*, **100**, 1066.
[56] Palmer, R. E., and Rous, P. J., 1992, *Rev. mod. Phys.*, **64**, 383.
[57] Dehmer, J. L., and Dill, D. 1978, *Phys. Rev.* A, **18**, 164.
[58] Golovin, A. V., Cherepkov, N.A., and Kuznetsov, V. V., 1992, *Z. Phys.* D, **24**, 371.
[59] Kaesdorf, S., Schönhense, G., and Heinzmann, U., 1985, *Phys. Rev. Lett.*, **54**, 885.
[60] Van Brunt, R. J., and Kieffer, L. J., 1970, *Phys. Rev.* A, **2**, 1293; 1970, *ibid.*, **2**, 1899.
[61] Spence, D., and Schulz, G. J., 1970, *Phys. Rev.* A, **2**, 1802; Wong, S. F., Boness, M. J. W., and Schulz, G. J., 1973, *Phys. Rev. Lett.*, **31**, 969.
[62] Steinfeld, J. I., Adler-Golden, S. M., and Gallagher, J. W., 1987, *J. Phys. Chem. Ref. Data*, **16**, 911.
[63] Anderson, S. M., and Mauersberger, K., 1995, *J. Geophys. Res.*, **100**, 3033.
[64] Levene, H. B., Nieh, J.-C., and Valentini, J. J., 1987, *J. chem. Phys.*, **87**, 2583; Kinugawa, T., Sato, T., Arikawa, T., Matsumi, Y., and Kawasaki, M., 1990, *J. chem. Phys.*, **93**, 3289; Daniels, M., and Wiesenfeld, J. R., 1993, *J. chem. Phys.*, **98**, 321; Suits, A. G., Miller, R. L., Bontuyan, L. S., and Houston, P. L., 1993, *J. Chem. Soc. Farad. Trans.*, **89**, 1443; Thelen, M.-A., Gejo, T., Harrison, J. A., and Huber, J. R., 1995, *J. chem. Phys.*, **103**, 7946; Stranges, D., Yang, X., Chesko, J. D., and Suits, A. G., 1995, *J. chem. Phys.*, **102**, 6067.
[65] Swanson, N., and Celotta, R. J., 1975, *Phys. Rev. Lett.*, **35**, 783.
[66] Allan, M., Mason, N. J., and Davies, J. A., 1996, *J. chem. Phys.*, **105**, 5665; Mason, N. J., Gingell, J. M., Davies, J. A., Zhao, H., Walker, I. C., and Siggel, M. R. F., 1996, *J. Phys.* B, **29**, 3075.
[67] Allan, M., Asmis, K. R., Popovic, D. B., Stepanovic, M., Mason, N. J., and Davies, J. A., 1996, *J. Phys.* B, **29**, 4727; Walker, I. C., Gingell, J. M., Mason, N. J., and Marston, G., 1996, *ibid.*, **29**, 4749.
[68] Skalny, J. D., Matejcik, S., Kiendler, A., Stamatovic, A., and Märk, T. D., 1996, *Chem. Phys. Lett.*, **255**, 112.
[69] Novick, S. E., Engelking, P. A., Jones, P. L., Futrell, J. H., and Lineberger, W. C., 1979, *J. chem. Phys.*, **70**, 2652.
[70] Wang, L. J., Woo, S. B., and Helmy, E. M., 1987, *Phys. Rev.* A, **35**, 759.
[71] Arnold, D. W., Xu, C., Kim, E. H., and Neumark, D. M., 1994, *J. chem. Phys.*, **101**, 912.
[72] Locker, J. R., Joens, J. A., and Blair, E. J., 1987, *J. Photochem.*, **36**, 235.
[73] Lee, T. J., 1990, *Chem. Phys. Lett.*, **169**, 529.
[74] Xantheas, S. S., Atchity, G. J., Elbert, S. T., and Ruedenberg, K., 1991, *J. chem. Phys.*, **94**, 805.
[75] Hay, P. J., and Dunning, Jr., T. H., 1977, *J. chem. Phys.*, **67**, 2290.

[76] Banichevich , A., and Peyerimhoff , S. D., 1993, *Chem. Phys.*, **174**, 93.
[77] Bouvier , A. J., Bacis, R., Bussery , B., Churassy , S., Inard , D., Nota , M., Brion , J., Malicet , J., and Anderson , S. M., 1996, *Chem. Phys. Lett.*, **255**, 263.
[78] Tsuneda , T., Nakano , H., and Hirao , K., 1995, *J. chem. Phys.*, **103**, 6520.
[79] Borowski , P., Fulscher , M., Malmqvist , P., and Roos, B. O., 1995, *Chem. Phys. Lett.*, **237**, 195.
[80] Braunstein , M., Hay, P. J., Martin , R. L., and Pack , R. T., 1991, *J. chem. Phys.*, **95**, 8239.
[81] Braunstein , M., and Pack , R. T., 1992, *J. chem. Phys.*, **96**, 6378.
[82] Anderson , S. M., Hupalo , P., and Mauersberger ,K., 1993, *J. chem. Phys.*, **99**, 737.
[83] Minaev , B., Ågren , H., 1994, *Chem. Phys. Lett.*, **217**, 531.
[84] Braunstein , M., Martin , R. L., and Hay, P. J., 1995, *J. chem. Phys.*, **102**, 3662.
[85] Gole, J. L., and Zare, R. N., 1972, *J. chem. Phys.*, **57**, 5331.
[86] Garner , M. C., Sherwood , C. R., Hanold , K. A., and Continetti , R. E., 1996, *Chem. Phys. Lett.*, **248**, 20.
[87] Levene , H. B., and Valentini , J. J., 1987, *J. chem. Phys.*, **87**, 2594.
[88] Schinke , R., 1993, *Photodissociation Dynamics* (Cambridge: Cambridge University Press) pp. 251–255.
[89] Castleman , A. W., and Bowen , K. H., 1996, *J. phys. Chem.*, **100**, 12911.
[90] Lifshitz , C., 1993, *Cluster Ions*, edited by C. Y. Ng, T. Baer and I. Powis (New York: John Wiley) pp. 121–164.
[91] Bastian , M. J., Dressler , R. A., Levandier , D. J., Murad , E., Muntean , F., and Armentrout , P. B., 1997, *J. chem. Phys.*, **106**, 9570.
[92] Anderson , S. L., 1994, *Clusters of Atoms and Molecules II*, edited by H. Haberland (Berlin: Springer-Verlag) pp. 241–259.
[93] Coe, J. V., Snodgrass , J. T., Freidhoff , C. B., McHugh , K. M., and Bowen , K. H., 1987, *J. chem. Phys.*, **87**, 4302.
[94] Hiraoka , K., Fujimaki , S., Aruga , K., and Yamabe , S., 1994, *J. phys. Chem.*, **98**, 8295.
[95] Siegel , M. W., Celotta , R. J., Hall , J. L., Levine , J., and Bennett , R. A., 1972, *Phys. Rev.* A, **6**, 607.
[96] Massey , H. S. W., 1976, *Negative Ions* 3rd edition (Cambridge: Cambridge University Press) pp. 191–194.
[97] Yang , X., Price , J. M., Mack , J. A., Morgan , C. G., Rogaski , C. A., McGuire , D., Kim , E. H., and Wodtke , A. M., 1993, *J. Phys. Chem.*, **97**, 3944.
[98] Hopper , D. G., Wahl , A. C., Wu, R. L. C., and Tiernan , T. O., 1976, *J. chem. Phys.*, **65**, 5474.
[99] Ferguson , E. F., Fehsenfeld , F. C., and Schmeltekopf , A. L., 1967, *J. chem. Phys.*, **47**, 3085.
[100] Coe, J. V., Snodgrass , J. T., Freidhoff , C. B., McHugh , K. M., and Bowen , K. H., 1986, *Chem. Phys. Lett.*, **124**, 274.
[101] Gorden , R., and Ausloos , P., 1965, *J. Res. Nat. Bur. Std.* A, **69**, 79.
[102] Parnis , J. M., Hoover , L. E., Pedersen , D. B., and Patterson , D. D., 1995, *J. phys. Chem.*, **99**, 13528.
[103] Chantry , P. J., 1969, *J. chem. Phys.*, **51**, 3369.
[104] Papai , I., and Stirling , A., 1996, *Chem. Phys. Lett.*, **253**, 196.
[105] Takatsuka , K., 1997, *Phys. Rev.* A, **55**, 347.
[106] Balint-Kurti , G. G., and Schatz , G. C., 1997, *J. Chem. Soc. Faraday Trans.*, **93**, 755.
[107] Hanold , K. A., Luong , A. K., and Continetti , R. E., work in preparation.
[108] Maul , C., and Gericke , K. H., 1997, *Int. Rev. phys. Chem.*, **16**, 1.